Nonlinear Optical Signal Processing and Tunable Optical Delays in Silicon-on-Insulator Waveguides

Mina Spasojevic

Department of Electrical & Computer Engineering
McGill University
Montreal, Canada

August 2013

A thesis submitted to McGill University in partial fulfillment of the requirements of the degree of Master of Engineering.

Abstract

The continued trend of increasing demand for large communications bandwidths is placing great strain on today's communications technology. This underlines the need for improving capacities and scalability of the existing as well as the future transmission systems. Investigating the capabilities of different modulation formats presents one way of addressing the matter. This thesis explores the optical time-division (de)multiplexing (OTDM) modulation scheme and provides a platform for building an all-optical signal processing system in silicon-on-insulator (SOI) relying on OTDM. It demonstrates successful OTDM demultiplexing and tunable optical delays both implemented in silicon nanoscale optical devices.

OTDM demultiplexing is carried out by exploiting the nonlinearities in silicon waveguides. It focuses on four wave mixing (FWM) phenomenon chosen for its great potential for very high data rates resulting from its instantaneous nature, in addition to the advantage of being transparent to modulation formats. The thesis demonstrates how all-optical OTDM demultiplexing can be achieved through a two step process, generation of continuously tunable delay line followed by demultiplexing process, with both steps implemented in the same silicon waveguide. It demonstrates successful 40 Gb/s-to-10 Gb/s demultiplexing resulting in four error free demultiplexed channels.

For further integration of the demultiplexing process, this thesis explores achieving tunable optical delays in silicon waveguides. It shows two approaches for implementing sidewall grating structures, serial Bragg grating arrays and the step-chirped Bragg gratings. Both approaches were fabricated and characterized and demonstrate relatively large delays (up to 65 ps) in discrete steps (from 15 ps to 32 ps) over wide bandwidths (from 35 nm to 70 nm), however they require further optimization.

All-optical signal processing and optical devices presented in this thesis provide building blocks and indicate future steps that can lead toward fully integrated OTDM demultiplexer in SOI.

Sommaire

L'augmentation incessante de la demande pour de larges bandes passantes crée de grandes tensions sur les technologies de communications existantes. Cela met en évidence le besoin d'améliorer la capacité et l'extensibilité des systèmes de transmission existants et futurs. Cette question peut être résolue, entre autres, par l'exploration des capacités de formats de modulation différents. Cette thèse examine un schéma de (dé)multiplexage optique temporel (OTDM) et présente une plateforme pour la mise en place d'un système pour le traitement de signaux exclusivement optiques sur silicium sur isolant (SOI) qui s'appuie sur le démultiplexage OTDM. Le démultiplexage OTDM et les délais optiques réglables, tous deux implémentés sur des dispositifs en silicium à l'échelle nanométrique, sont démontrés avec succès.

Le démultiplexage OTDM est effectuée par l'exploitation de la non-linéarité des guides d'onde sur silicium. Cette technique emploie le phénomène de mélange à quatre ondes (FWM) choisi pour son potentiel pour les très hautes fréquences de données grâce à sa nature instantanée en plus de posséder l'avantage d'être transparent aux formats de modulation. Cette thèse démontre que le démultiplexage OTDM exclusivement optique peut être effectué en deux étapes, la production de ligne à retard ajustable en continue suivit par un procédé de démultiplexage, tous deux implémentés dans le même guide d'onde sur silicium. Un démultiplexage de 40 Gb/s à 10 Gb/s résultant en quatre canaux démultiplexés sans erreur est démontré avec succès.

Pour une intégration plus poussée du procédé de démultiplexage, cette thèse examine la possibilité de créer un délai optique ajustable dans les guides d'onde sur silicium. Deux approches pour la mise en oeuvre de réseaux sur les parois d'un guide d'onde sont démontrées: une série de réseaux de Bragg et des réseaux de Bragg chirpés. Les deux approches ont été fabriquées et caractérisées et démontrent des délais relativement larges (jusqu'à 65 ps) par étapes discontinues (de 15 ps à 32 ps) sur une bande passante large (de 35 nm à 70 nm). Ces approches doivent cependant être davantage optimisées.

Le traitement de signaux exclusivement optique et les dispositifs optiques présentés dans cette thèse fournissent les étapes et les informations nécessaires qui pourraient mener à un démultiplexeur OTDM sur silicium complètement intégré.

Acknowledgments

For completing my masters degree I owe sincere gratitude to my supervisor Prof. Lawrence R. Chen for his endless encouragement, support and guidance through the research that was conducted and valuable knowledge that was gained. His patience, knowledge, and motivation have had a valuable positive influence to the work accomplished. It was a great pleasure to work with him.

I would also like to thank many colleagues whose help was critical in important moments during experimental and theoretical work: Mohammad Rezagholipour Dizaji, Jia Li, Alireza Nezam-Alhosseini, Pegah Seddighian, Raja Ahmad, Sandrine Filion Côté and all the other people that helped on various occasions. Special thanks go to Tianye Huang who guided me through early experimental steps.

For implementing and testing the silicon-on-insulator based devices I would like to acknowledge the NSERC NGON CREATE program, the NSERC SiEPIC CREATE program and Passive Silicon Photonics workshop for their support, CMC Microsystems for fabrication assistance, Lumerical Solutions and Mentor Graphics for design software, Richard Bojko at the University of Washington and University of Washington Microfabrication/Nanotechnology User Facility for fabrication, Prof. Lukas Chrostowski and Dr. Dan Deptuck for instructions during the Passive Silicon Photonics workshop, and Valentina Donzella at University of British Columbia for recording the preliminary experimental results of fabricated devices.

I would also like to thank the entire Photonic Systems Group (PSG) and SYTACom staff for their valuable assistance, and NSERC and McGill University for their support.

Special thanks go to members of my family who always believed in me and to McGill Students Outdoors Club that provided memorable experience outside the research environment.

Mina Spasojevic

Contents

List of Figures

List of Tables

List of Acronyms

ADC	Analog-to-Digital Converter
ASE	Accumulated Spontaneous Emission
AWG	Arrayed Waveguide Grating
B2B	Back to Back
BER	Bit Error Rate
BERT	Bit Error Rate Tester
BPF	Band Pass Filter
CAGR	Compound Annual Growth Rate
CE	Conversion Efficiency
CMOS	Complementary MetalOxideSemiconductor
CW	Continuous Wave
DAC	Digital-to-Analog Converter
DCA	Digital Communication Analyzer
DFB	Distributed Feedback Structure
DPSK	Differential Phase Shift Keying
DSP	Digital Signal Processing
DWDM	Dense Wavelength Division Multiplexing
E/O	Electro Optic
EAM	Electro-absorption Modulator
EDFA	Erbium Doped Fibre Amplifier
ETDM	Electrical Time Division Multiplexing
FBG	Fiber Bragg Grating
FWM	Four Wave Mixing
HNLF	Highly Nonlinear Fiber

IC	Integrated Circuit
ICT	Information and Communication Technology
IM/DD	Intensity Modulation with Direct Detection
IMEC	Interuniversity Microelectronics Centre
IP	Internet Protocol
MLL	Mode Lock Laser
MPW	Multi-Project Wafer Shuttle
MZM	Mach-Zehnder Modulator
NGON	Next Generation Optical Networks
NOLM	Nonlinear Optical Loop Mirror
NSERC	Natural Sciences and Engineering Research Council
O/E	Opto Electronic
OFDM	Orthogonal Frequency Division Multiplexing
OLO	Optical Local Oscillator
OMUX	Optical Multiplexer
OOK	On Off Keying
OSA	Optical Spectrum Analyzer
OSNR	Optical Signal to Noise Ratio
OTDL	Optical Tunable Delay Line
OTDM	Optical Time Division Multiplexing
PD	Photo Detector
PLC	Planar Lightwave Circuit
PON	Passive Optical Network
PRBS	Pseudo Random Bit Sequence
QAM	Quadrature Amplitude Modulation
QPSK	Quadrature Phase Shift Keying
RODM	Reconfigurable Optical Add/Drop Multiplexer
RZ	Return to Zero
SC	Supercontinuum
SNR	Signal to Noise Ratio
SOA	Semiconductor Optical Amplifier
SOI	Silicon on Insulator
SPM	Self Phase Modulation

TDM	Time Division Multiplexing
TE	Transverse Electric
THG	Third Harmonic Generation
TM	Transverse Magnetic
TMM	Transfer Matrix Method
TPA	Two Photon Absorption
VNI	Visual Networking Index
VOA	Variable Optical Attenuator
WBG	Waveguide Bragg Grating
WDM	Wavelength Division Multiplexing
XAM	Cross Absorption Modulation
XGM	Cross Gain Modulation
XPM	Cross Phase Modulation

Chapter 1

Introduction

1.1 Motivation for Increased Channel Capacity

Emerging internet and digital technology have changed the way people interact today. Digital culture embraces intensive video-oriented services used in communications, education, entertainment, healthcare, business, etc. Digital consumers are accessing many types of multimedia content through their PCs, phones, television or through other emerging "smart" mobile devices. Computers are used as phones, mobile devices are used as television, while television is used for things such as high definition time-shifted TV programming [1]. Such services have been integrating voice, video and data through internet protocols (IP) and are hungry for bandwidth in order to satisfy demands of increasing number of users. The world's total internet usage statistics show a growth of 566.4 % in the period from 2000 to 2012 [2] while supporting some of many communication services people rely on today and projected to evolve further in the following years, i.e. Voice over IP (VoIP), mobile video, desktop videoconferencing and others (Table 1.1). Two main factors affect this unparalleled growth, the increasing number of users and the increasing number of user devices enabling access to global networks.

In the period from 2011 to 2016, the residential and the business internet users are projected to grow to 2.3 billion each, while mobile consumers will grow to 4.5 billion [3]. For supporting service, it is forecasted that there will be up to 15 billion connected devices by 2015 [4, 5] with predictions of up to 50 billion by 2020 [6]. With this many devices and users the network architecture needs to continue expanding to support the growth in data traffic. Thus it is essential that systems not only improve high performance computa-

Residential Services	Consumer Mobile Services	Business Services
Digital TV	Consumer Short Message Service (SMS)	Room-based videoconferencing
Time-delayed TV	Consumer Multimedia Message Service (MMS)	Desktop videoconferencing
Video on demand (VoD)	Consumer mobile email	Audio conferencing
Voice over IP (VoIP)	Mobile gaming	Business IM
Consumer instant messaging (IM)	Mobile music	Web conferencing without video
Online gaming	Mobile video	Business IP telephony
Online music	Mobile social networking	Business mobile location-based services (LBS)
Online video	Consumer mobile LBS	Business mobile email
Social networking	Mobile commerce	Business mobile SMS

Table 1.1 Cisco VNI service adoption forecast categories and services [3].

tional abilities, but also enable data to flow faster to the end users as well as increase the bandwidth within the data centers [4]. To highlight the importance of data center traffic growth, Cisco analyzed and forecasted global data center IP traffic until 2016 and came up with astonishing numbers (Figure 1.1). While the amount of traffic crossing the internet networks was around 175 exabytes[1] in 2010, it is projected to reach 1.3 zettabytes[1] per year in 2016; moreover, the amount of global data center IP traffic is already 2.6 zettabytes per year and is projected to grow to 6.6 zettabytes in 2016 [7].

Information provided to users whether based on mobile devices or fixed ethernet network accounts for 17 percent of global data traffic. Reducing any delays in delivering information packets to end users requires high performance computations within the data center itself which accounts for 76 percent of data center traffic [7]. With these projections, servers within data centers will increase in growth 10 times by 2015 according to [5] which with today's technology would require building 45 new coal power plants to support 2015 IT infrastructure [8]. It becomes obvious to assume that to make this infrastructure scalable, the performance, energy efficiency and I/O bandwidth all play the key requirements in further development. Larger bandwidth is necessary to support the service demands, but advances in information technology, storage architectures, server clustering and new forms of information delivery all strive toward simplifying data center operations to reduce size, complexity and cost. A single infrastructure that can carry all kinds of traffic from fixed, mobile to photonics is desired [6]. Photonics based platforms were made possible

[1] http://www.cisco.com/assets/cdc_content_elements/networking_solutions/service_provider/visual_networking_ip_traffic_chart.html

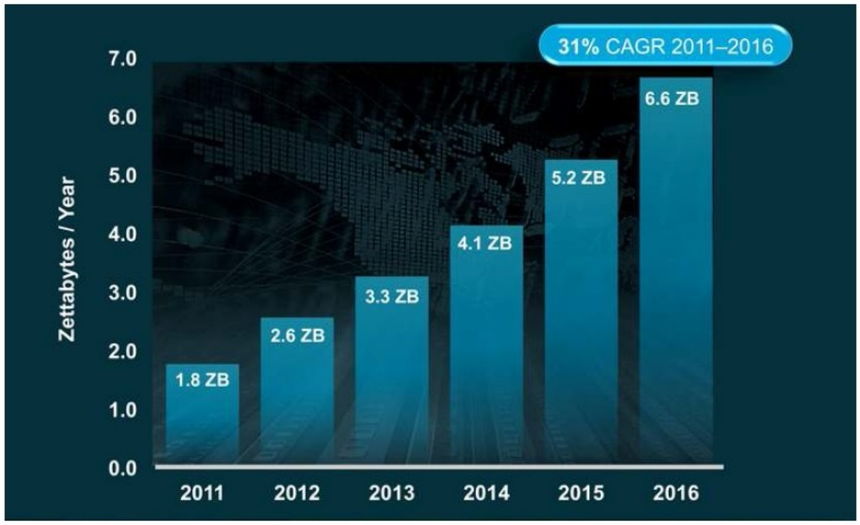

Fig. 1.1 Global data center IP traffic growth from 2011 to 2016 [7]. CAGR: compound annual growth rate.

by continuous development of higher performance devices and components: low-loss optical fibers, semiconductor lasers, detectors, multiplexing and demultiplexing ICs, arrayed waveguide gratings (AWG) and optical filters [9]. These led to advances in technologies such as wavelength division multiplexing (WDM), coherent optical communications, dynamically reconfiguration networks (i.e. reconfigurable optical add drop multiplexers or ROADMs) and long-haul transmission systems all proving that solutions to many of the previously mentioned concerns can be found in next generation optical networks, as has already been illustrated [10, 11].

1.2 Optical Signal Processing Schemes for Increasing Capacity: WDM, OTDM, Coherent Communications

Promising prospects of high transmission rates in the optical communication systems come from high frequency range of the optical carrier waves (around 200 THz). The bandwidth of the modulated carrier can be up to a few percent of the carrier frequency. This means that, in principle, optical communication systems have the potential of carrying information at up to 10 Tb/s [12]. Ethernet through optical fibers as a low-cost point-to-multipoint fiber infrastructure supporting gigabit per second speeds started emerging in 2002 [13].

Currently, commercial optical systems can operate at up to bit rates of 100 Gb/s [10] indicating there is a lot of room for improvement. The commercial systems have been limited by dispersive and nonlinear effects in the fibers as well as by the speed of the electronic components.

There have been a few modulating schemes proposed to extend the rate beyond these limitations. Optical signal that is used as a carrier is characterized by intensity, amplitude, frequency, phase and polarization. Modulating any of these properties can improve transmission but at the expense of different complexity levels and all the necessary equipment. It can also allow transmission of multiple signals simultaneously referred to as multiplexing.

The simplest modulation scheme is intensity modulation with direct detection (IM/DD) where the electrical signal modulates the intensity of the optical carrier transmitting the optical signal that is then directly detected by the receiver before being converted back to the electrical signal. IM/DD can employ multiplexing in time or in frequency domain which are referred to in optics as optical time-division multiplexing (OTDM) and wavelength division (WDM) multiplexing.

1.2.1 WDM Systems

In WDM systems (Figure 1.2) multiple optical carriers at different wavelengths are modulated by independent electrical signals. This forms multiple channels in which multiple optical signals can be simultaneously transmitted through the same fiber. The signals are combined using optical multiplexers. This combined optical signal is then demultiplexed at the receiver into separate channels at different wavelengths that are sent to different detectors. Such a scheme can potentially exploit large bandwidth in fibres (1300 nm - 1550 nm) by allowing transmission of hundreds of channels that could be spaced less than a nanometer apart (i.e. 100 GHz spacing). The invention of the coherent optical source and low loss optical fiber in the 1970s and erbium-doped-fibre-amplifier (EDFA) in the 1980s propelled WDM systems as being the simplest form to implement and are still the most extensively commercially used today.

1.2.2 OTDM Systems

In OTDM systems (Figure 1.3) multiple optical signals can also be simultaneously transmitted through the same fiber, but sharing the same optical carrier. Optical signals at the

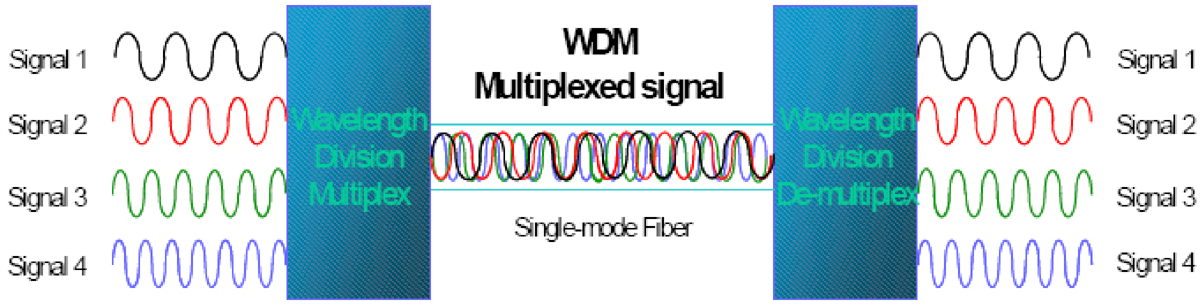

Fig. 1.2 Wavelength division multiplexing block diagram (figure taken from http://fiberoptic101.blogspot.ca/2010/11/signal-multiplexing.html).

same bit rate are multiplexed optically to form a combined bit stream. If there are N input optical signals, the combined signal has N times the bit rate of one input signal and is comprised of N channels; every consecutive bit in each interval belongs to a different channel. This signal is then demultiplexed at the receiver not based on different wavelengths, as it was the case in WDM, but based on the arrival time of the bits. Such a scheme can further exploit the large bandwidth in fibres if implemented with WDM systems. Namely, each signal carried on a different wavelength could be time division multiplexed as well. If there are M different carriers this allows the transmission of not only M $\times$ WDM channels, but also N $\times$ OTDM channels with every wavelength, thus scaling the transmission capacity to large magnitudes.

WDM systems become limited with their transmission bandwidth and the channel count. OTDM technique proved to be a simple method for increasing the bit rate within a channel. However, coherent crosstalk between adjacent pulses with the same wavelength easily occurs if the pulsewidth of the pulses is not narrow enough. Thus, OTDM systems require more complex transmitter and receiver platforms capable of producing ultra-short pulses as well as switching at high repetition rates in order to distinguish all the channels. They haven't been used commercially as widely as WDM systems. Though, with emerging technology, they have been recently gaining more popularity due to their spectral efficiency along with the high bit rate capabilities.

1.2.3 Coherent Communication Systems

WDM and OTDM are both IM/DD modulation schemes, they do not preserve any information about phase. Coherent communication systems transmit the signal by modulating

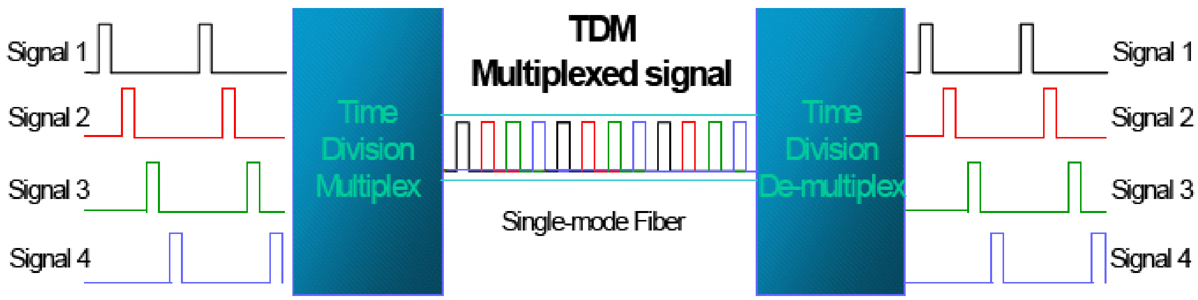

Fig. 1.3 Time division multiplexing block diagram (figure taken from http://fiberoptic101.blogspot.ca/2010/11/signal-multiplexing.html).

amplitude, phase and polarization of the optical carrier instead of just amplitude. The systems' backbone relies on complex digital signal processing (DSP) algorithms for high speed phase estimation and fast switching electrical components for electrical to digital conversion both needed for detecting the transmitted signal. In principle, a transmitted optical signal is combined with the local oscillator and based on their superposition, detection is performed [12]. Coherent detection can be analyzed through four subsystems (Figure 1.4). Optical front end that linearly maps the optical signal into a set of electrical signals; analog to digital converters (ADC) that then convert the electrical signals into a set of discrete-time-quantized signals; digital demodulation of the quantized signals; and complex digital signal processing algorithms designed for any error correction of the demodulated signals and electronic compensation of transmission impairments [14]. The DSP part of the coherent detection consists of multiple correction subsystems implementing functionalities such as carrier phase estimation, de-skewing, orthogonalization, digital equalization, timing recovery, and others [14]. Coherent optical communication was introduced with WDM systems, but didn't gain as much popularity due to complexity required in electrical circuit components and extensive digital signal processing algorithms needed for detecting. In recent years progress in the integrated circuit fabrication and DSP technologies made coherent detection an attractive form of modulation, especially when incorporated with other forms of modulation. It brought advantages such as high spectral and power efficiency, reduced electrical bandwidth and reduced cost, increased tolerance to chromatic and polarization mode dispersion.

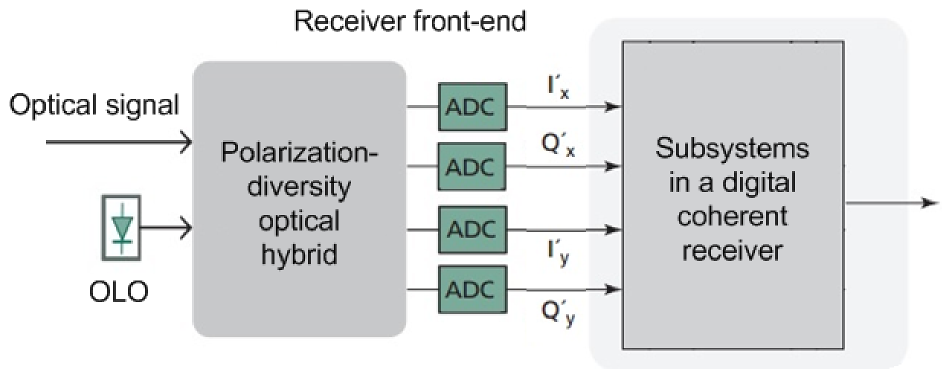

Fig. 1.4 Block diagram of a coherent receiver. OLO: optical local oscillator, ADC: analog to digital converter.

1.2.4 Projection of WDM, OTDM and Coherent Detection

Global IP network has tremendously grown in complexity and cost over years and establishing a scalable and affordable backbone for future development that would support the traffic growth, plays a key role today. Research has been focusing on new network technologies, architectures and protocols with significant work done in optical domain for its promising transmission capacities and bit rates. Figure 1.5 summarizes the trends in transmission capacities for research and commercial systems since the inventions of low loss fibers, coherent optical sources and EDFAs. Though advances in high-speed electronic signal processing components propelled the development of coherent detection, the optical link remained a crucial backbone in these systems. Coherent communication systems involve many electrical and software based components that consume power and their digital integration as well as improved algorithms supporting complexity have been highly desired and researched. Additionally, coherent detectors are limited by the photodetector's bandwidth and the speed of the analog to digital converters. Thus, combining modulation formats such as WDM and OTDM with the coherent detection can push the capacities even further. The data rate increases by increasing the symbol rate which can then be further increased by advanced modulation of large number of bits encoded per symbol [15].

OTDM transmission technology is defined by its ultrafast optical signals enabling high symbol rates up to a range of a terabaud. When such a system is combined with coherent detection (Figure 1.6) very high serial data rates in a single wavelength channels can be achieved (i.e. in [15] 10.2 Tb/s was recorded over 29 km dispersion managed fiber). Keeping

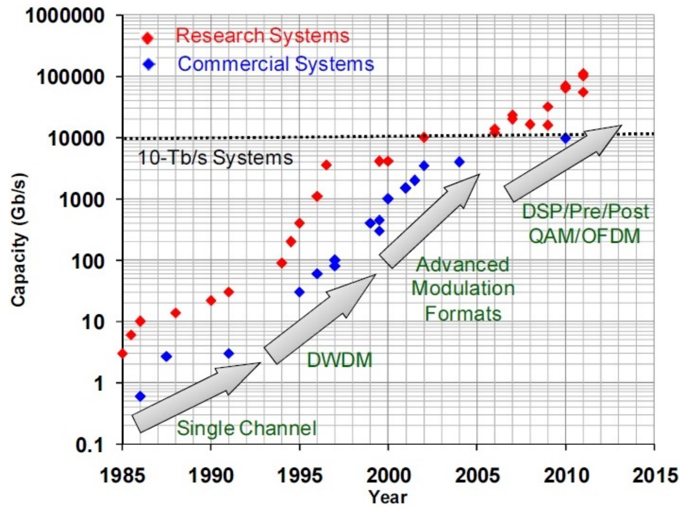

Fig. 1.5 The trend of capacity versus year for optical fibre transmission systems [16]. DWDM: dense wavelength division multiplexing, DSP: digital signal processing, QAM: quadrature amplitude modulation, OFDM: orthogonal frequency division multiplexing.

in mind that electrical time division multiplexing (ETDM) symbol rates have reached the 100 GBd regime, while optical time division multiplexing symbol rates reached 1.28 Tbd (serial data rates of up to 10.2 Tb/s in a single wavelength channel) [15], one can see that further research in OTDM technology, with its high serial data rates capacity, still promises advances in data rates used as a standalone system or combined with other modulation formats.

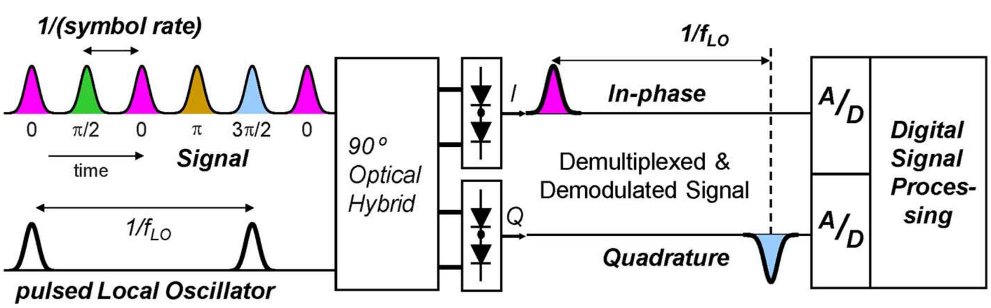

Fig. 1.6 Principle of synchronous digital coherent demultiplexer of a single polarization signal. The demultiplexing is shown for one tributary only as it is typical for laboratory experiments [15]. © 2012 IEEE

1.3 All-Optical Signal Processing and Green Networks

Supporting the internet traffic growth through advances in network technology and architecture requires an increase in the number of power hungry equipment. Just the core of the network housing growing data centers requires energy consuming air conditioning units to sustain their high-performance operations [17]. Consequently, more detailed studies have been conducted on the impact of the Information and Communication Technology (ICT) on the total consumed electricity in the world. In 2009, ICT consumed about 8 % of the total electricity all over the world [18]. Figure 1.7 forecasts more than doubling of energy consumption of telecom networks by 2017, thus proving that reducing this consumption could have a significant impact in the future.

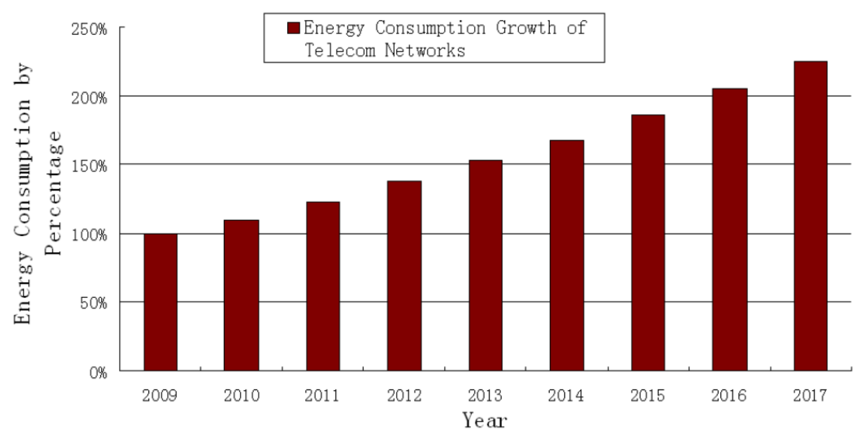

Fig. 1.7 Energy consumption forecast of telecom networks [18]. © 2010 IEEE

Two main approaches have been taken in realizing the reduction, focusing on renewable energies and building low energy equipment which makes increasing interest in energy efficient optical networks not surprising. Optical components consume low energy and optical transceivers are highly energy efficient [18]. Figure 1.8 demonstrates how the use of the optical networks would improve the total network power consumption by 15 % by 2025 while highlighting that high efficiency passive optical network (PON) components play an important role in future energy consumption. With this 15 % improvement the total network power consumption in 2025 would account for about 7 % of the 2010 global electricity supply, while without improvement it would account for about 75 % of the 2010 global electricity supply [19].

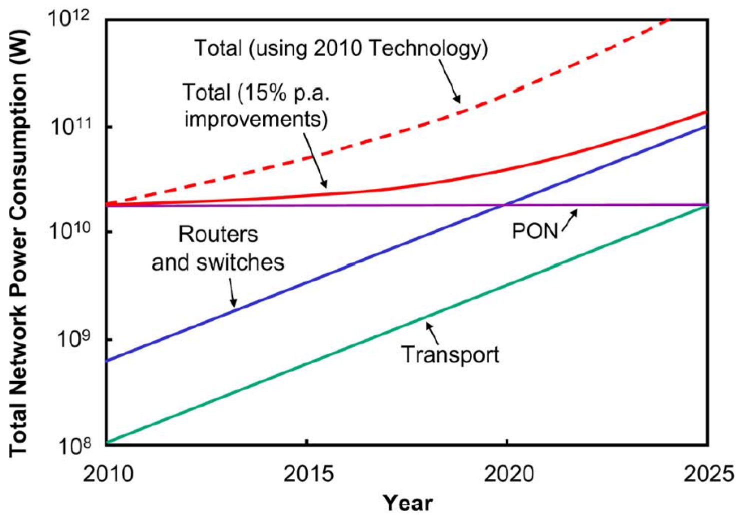

Fig. 1.8 Total power consumption of the network based on analysis assuming a 15 % p.a. improvement in equipment energy efficiency [19]. © 2011 IEEE

Optical networks can be implemented through different architectures involving optical switches, electronic switches, optical to electrical (O/E) and electrical to optical (E/O) signal conversion circuits, electrical modulation and optical modulation schemes, etc [18]. Commercially used WDM transmission network relies on multiplexers and demultiplexers, power amplifiers and O/E and E/O circuits for processing the signals for every wavelength used across the optical link, significantly contributing to the power consumption. Additionally, the complexity of the electronic circuits required for high-speed switching is approaching the inherent limitations in speed affecting their performance. This encourages research to investigate high speed all-optical signal processing networks that could bypass electronic circuits, reduce the number of switches and routers in the network while being transparent to the increasing bit rate. With growing transmission rates high spectral efficiency that can be achieved in all-optical networks also becomes a useful strategy to improve energy efficiency simply because it minimizes the number of amplifiers required. Thus, even though there still are and will be efforts to improve electronic circuits and reconfigure the communication networks, all-optical signal processing shows a promising potential to overcome many power and speed related obstacles in the future.

1.4 All-Optical Signal Processing in OTDM Systems: Brief Overview of Necessary Technologies and Signal Processing Approaches

Major application of all-optical signal processing has been demonstrated in OTDM systems [20]. To be implemented, such systems require ultrafast all-optical devices. Some of the key techniques employed in OTDM network systems include multiplexing, clock recovery and optical demultiplexing schemes that have been heavily investigated in all-optical domain. Figure 1.9 shows the schematic diagram of these key components. In the transmitter side, ultrafast pulses are generated by a mode locked laser that are then modulated, multiplied and interleaved in time with an array of delay-lines to obtain a combined, higher bit rate signal. This signal is then compressed or shaped if necessary and transmitted. Optical repeater is there to compensate for any propagation losses or for dispersion effects while in the transmission medium either through 2R function (re-amplification and re-shaping), or 3R function (2R + re-timing). The signal is received with demultiplexing circuit, where clock recovery is necessary to extract clock timing out of the incoming data signals. Multiplexing and demultiplexing circuits can be implemented through many different techniques focusing on optical nonlinearities in semiconductor-based and fiber-based devices [20, 21].

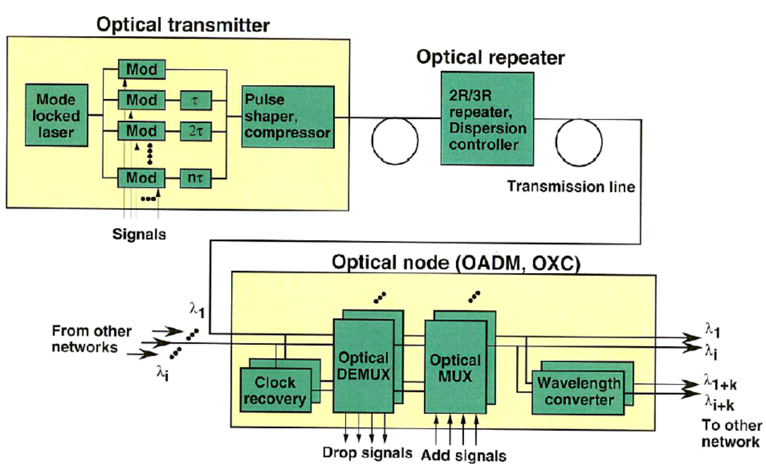

Fig. 1.9 Simplified schematic diagram of the OTDM network system. Optical transmitter generates optical data signals that travel through the transmission lines and optical repeaters before being received by the optical node [20]. © 2004 IEEE

1.5 The Significance of Reducing the Print Size

In the never-ending quest for increased data rate capacity, the size of the systems started to play a big role from the mid 2000s. For instance, today's internet traffic in the United States requires routers and switches that are very large in size; the highest-capacity commercial routers being sold by CISCO for the core network come in 1,152 slots of line cards in 80 shelves, consuming 0.85 MW in power and weighing 56,656 kg [22]. Consequently, power consumption and size pose a limiting factor in scalability of such systems. But further reducing the size of the electronic integrated circuits and electrical components to enable scalability started affecting their transmission capabilities due to current leakages and heat dissipations. The idea of using photons instead of electrons to carry information has been around since 1980s but the necessary technology to implement optics in such complex systems was not developed. Integrating optic devices required extending beyond optical fibers and fiber based equipment and transferring onto planar substrates, similar to conventional electronics. Recent developments [22, 23] gave rise to photonic integration that could offer solution to many of the above mentioned problems. Nevertheless, photonic integration can still be very challenging and costly as fabrication processes for many discrete devices are still specialized for intended purposes. Solution to this problem started appearing in the field of silicon photonics. Despite silicon not being the material of choice for many applications, its compatibility with CMOS technology motivates in depth research and development of integrated components based on silicon by exploiting mature and existing IC industry. High optical mode confinement due to high index contrast between silicon ($n = 3.45$) and silica (SiO2) ($n = 1.45$) allows for low loss propagation in very small feature sizes. Coupling, switching, splitting, multiplexing and demultiplexing of optical signals can all be implemented in nanometer scale silicon waveguides with minimal losses [24].

1.6 Motivation and Thesis Objectives

There are multiple solutions to answer the demand for high data rate capacity with different modulation techniques (WDM, OTDM, coherent communications), different device technologies (electro-optic devices, all-optical devices) and different platforms (fiber or semiconductor based, silicon on insulator (SOI)) and all of them require different cost and levels of complexity. The incentive of the work described here is to explore approaches and techniques in all-optical signal processing for OTDM networks. The motivation behind investigating all-optical OTDM lies in its potential to offer bit rates of more than 1 Tb/s by bypassing the speed limitations of electronic components used in commercial transceivers. The main focus of the work is on optical demultiplexing part comprising of exploiting nonlinearities in silicon waveguides as well as on developing grating structures in SOI. The final incentive is to implement a compact, nanometer scale demultiplexing circuit on a photonic chip demonstrating advantages in a bit rate scalability and overall footprint.

This thesis will demonstrate successful, error free demultiplexing of 40 Gb/s OTDM data to 4×10 Gb/s channels through use of four wave mixing (FWM) phenomenon supported in silicon waveguides. Demultiplexing will be performed in two separate steps, where first the 10 GHz gating signal will be generated through a tunable delay line. The tunable delay line will be implemented through FWM in a silicon waveguide and consequently wavelength conversion process followed by the dispersion in a chirped fiber Bragg grating that introduces required time delay in gating signal. The second step will be actual demultiplexing of 40 Gb/s signal implemented through proper alignment of the gating signal and the lower rate tributary channel of the OTDM signal followed again by FWM in a silicon waveguide for channel extraction.

The thesis will also demonstrate a successful design of discretely tunable delay lines in silicon waveguides based on sidewall grating structures while achieving delays in steps of 14, 15, 20 and 32 ps over tens of nm bandwidths. Both silicon waveguides and waveguide gratings were designed as part of Silicon Nanophotonics Fabrication course and their performance was characterized and reported. With accomplished results in performance of the two separate devices their functions are visualized to be combined together and implemented in a single demultiplexing circuit in the future.

1.7 Thesis Outline

This thesis is organized as follows. Chapter 1 was dedicated to introduction and motivation for optical signal processing focusing on all-optical OTDM and nanometer scale silicon platforms.

Chapter 2: All-optical OTDM building blocks

This chapter introduces OTDM demultiplexing in different media: semiconductors, fibers and nanophotonic waveguide devices. It compares the reported results and data rates achieved in semiconductor optical amplifiers (SOAs), electro-absorption modulators (EAMs), highly nonlinear fibers (HNLFs), nonlinear optical loop mirrors (NOLMs) and nanophotonic waveguides. It also introduces the principles behind FWM phenomenon and how it can be exploited for tunable optical delay line generation and demultiplexing process.

Chapter 3: Experimental FWM based OTDM demultiplexing using SOI
The third chapter gives a brief overview of the previously achieved results when demultiplexing was implemented in HNLF with bidirectional propagation and through FWM. Furthermore, it introduces the characterization results of silicon waveguides to be used instead of HNLF. Finally, it describes in detail the implementation of the experimental setup when OTDM demultiplexing was performed in silicon waveguides, followed by the achieved results.

Chapter 4: Design and preliminary results on step-chirped and serial gratings in SOI
This chapter introduces Bragg gratings and their implementation in fiber and silicon. It gives the detailed parameters and describes the design used for fabrication of sidewall grating structures in SOI. It concludes with the characterization results achieved experimentally.

Chapter 5: Future work and conclusion
This chapter summarizes the work explained in this thesis followed by the future steps to be taken toward further integration.

Chapter 2

All-Optical OTDM Building Blocks

2.1 OTDM Multiplexing/Demultiplexing Techniques

The same bit rate optical signals can share the same carrier frequency by being multiplexed in time, meaning if they are interleaved in time N times they form a higher bit rate stream composed of N channels. The more interleaved signals, the higher the channel capacity. In order to interleave more signals, the optical sources have to be able to generate very short pulses, i.e. picoseconds transform-limited chirpless pulses at repetition rates ranging anywhere from 10 to 40 GHz [21]. However, depending on the final bit rate of the OTDM signal, the pulses may even need to be on the order of hundreds of femtoseconds. Such multiplexed signals therefore pose a tough requirement on the performance of the receiver heavily relying on good clock recovery schemes as well as high speed demultiplexing systems. All-optical demultiplexing has been demonstrated through various techniques in fiber based devices (HNLF, NOLM) and in semiconductor based devices (SOAs, EAMs) [25]. These devices are implemented in form of the fast switching mechanisms used to demultiplex high data rate signals and are often based on nonlinearity phenomena such as FWM and cross phase modulation (XPM). This thesis will focus on FWM process in HNLF and silicon waveguides, though a quick overview of other devices will be given as well.

2.2 FWM Background

The relation between polarisation P and electric field E is often linearly described when low power electric field is introduced into the medium. However, with increasing the power of E, this relation becomes nonlinear (Figure 2.1) and is characterized with new frequency generation. The relation can be expressed with

$$\mathbf{P} = \varepsilon_0 \left(\chi^{(1)} \cdot \mathbf{E} + \chi^{(2)} : \mathbf{EE} + \chi^{(3)} \vdots \mathbf{EEE} + \cdots\right) \tag{2.1}$$

where χ is the electric susceptibility of the medium and ε_0 is the permittivity of free space. When the electric field becomes strong enough the second ($\chi^{(2)}$) and higher order susceptibilities ($\chi^{(j)}$) become comparable to linear ($\chi^{(1)}$) and nonlinearities can be observed. Second order nonlinearity is significant only in non-centrosymmetric media, such as crystalline materials. Centrosymmetric media, such as silica glass found in typical optical fibers, experience third order nonlinearity while the second order completely vanishes. The media that experiences the nonlinear polarization due to only third order nonlinearities can be described with

$$\mathbf{P}_{NL} = \varepsilon_0 \ \chi^{(3)} \vdots \mathbf{EEE} \tag{2.2}$$

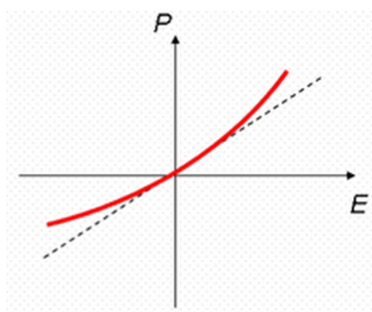

Fig. 2.1 The relation between the polarization and electric field in a nonlinear medium (figure taken from http://www.hcphotonics.com/ppxx.htm).

It is known that the refractive index (n) is related to susceptibility and the intensity of the field (I) as following

$$n = n_0 + n_2 I = \sqrt{1+\chi} \tag{2.3}$$

where n_2 is nonlinear refractive index. With refractive index being one of the fundamental defining properties of different materials, one can see that with introducing the strong electric field, not only does the polarization change, but many changes in the optical properties are also introduced. This combination can influence a number of new processes not present in linear regime, such as third harmonic generation[1], Kerr effect[2], two photon absorption[3] and FWM. Here we focus on FWM processes. If three electric fields are introduced into the medium of third order nonlinearity, FWM can occur. However, the conservation of energy and momentum needs to be satisfied for this process to take place. This is portrayed in Figure 2.2 showing that the frequencies (ω) and the wave vectors (k) between waves must be matched.

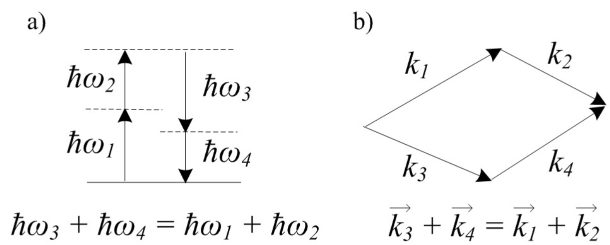

Fig. 2.2 Frequency (a) and phase (b) matching conditions.

Phase matching requirements are often easier met with terms of the form $\omega_x+\omega_y-\omega_z = \omega_{xyz}$, or $2\omega_x-\omega_z = \omega_{xxz}$ if two of the input signals have the same frequency. The latter form is referred to as degenerate FWM and is the most often occurring form. Figure 2.3 shows all the possible sums and differences in frequency generations with some of them occurring more readily than others, while also demonstrating a high chance of cross talk among the generated signals; something that often needs to be addressed in the communication systems relying on FWM.

The nonlinearity in materials prone to supporting FWM is often described with the nonlinear gain coefficient (γ) taking into account not only the nonlinear refractive index but also the effective area of the guiding medium (A_{eff}).

$$\gamma = \frac{\omega_0 n_2}{cA_{eff}} \tag{2.4}$$

The nonlinear coefficient is thus often referred to when characterizing the transmission media in communication systems. For how effective a particular medium is for FWM process, another term, conversion efficiency, is defined. FWM conversion efficiency (CE)

[1] Third harmonic generation (THG) is nonlinear process where three photons generate a single photon at three times the frequency
[2] Kerr effect is the intensity dependent refractive index change
[3] Two photon absorption (TPA) is the intensity dependent absorption

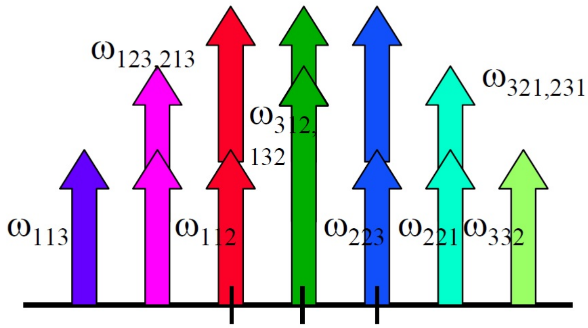

Fig. 2.3 FWM frequency generation (from the course notes of ECSE 527 Nonlinear Optics taught at McGill).

represents the measure of comparative power levels of existing and newly generated signals.

2.3 Demultiplexing of OTDM Signals Through FWM: Principle

High bit rate signals in OTDM systems require the pulsewidths of the input signal trains to be on the order of a picosecond or smaller. When the duty cycles[4] of these signals are kept small, they become an excellent choice for inducing nonlinearities in fibers or other media making use of high peak powers while keeping average power low. Figure 2.3 shows the generation of many new signals located at different frequencies. The consequence of signals mixing and generating new signals, as is the case with FWM, can be both beneficial and harmful in communication systems. In WDM systems it can induce crosstalk among the channels thus limiting the performance of the system. Though, the ultrafast nature of the nonlinear effects occurring could be used in fast signal processing schemes, specifically in wavelength conversion and demultiplexing of OTDM signals [26].

In degenerate FWM process (Figure 2.4) two signals at the same frequency ω_1 are mixed with the signal at different frequency ω_2 giving rise to the third signal at $\omega_3 = 2\omega_1 - \omega_2$. These are often referred to as the pump, the signal or probe and the idler, respectively.

FWM idler wave represents a wavelength converted replica of the signal. If OTDM signal consists of N multiplexed channels that are interleaved in time, a specific channel can be demultiplexed with the pump that is an optical pulse train at the bit rate of an individual channel. When the pump and the bit pattern of OTDM data signal associated with a single channel, overlap in time, FWM takes place and idler appears carrying the same

[4]The ratio of the pulsewidth and the bit window of the signal.

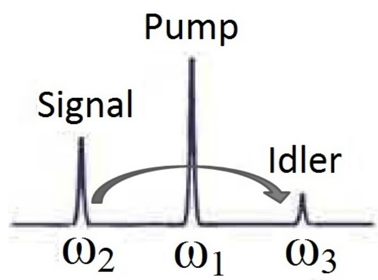

Fig. 2.4 Degenerative FWM.

information as the channel (except for the reversed phase), but at the different wavelength. Figure 2.5 demonstrates this concept in time domain, where, in this case, a 10 GHz pump at ω_1 is aligned with one of the four time slots in a 40 Gb/s data signal at ω_2. With the proper alignment of the 10 GHz pump and one of the tributaries' time slots (forming the peak with increased magnitude in Figure 2.5), a single OTDM channel can be wavelength converted from ω_2 to ω_3 and demultiplexed [26]. The pump signal is therefore sometimes referred to as an optical clock or gating signal. Aligning the clock signal can be achieved through many different optical delay schemes and devices successfully implemented in fiber or waveguide gratings [27].

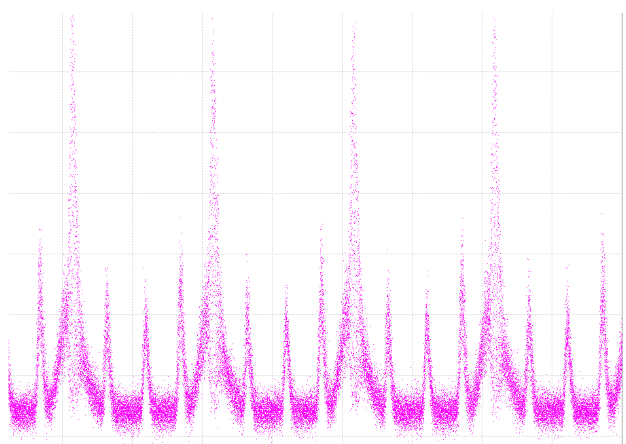

Fig. 2.5 10GHz gating signal time aligned with 40 Gb/s OTDM signal.

A demultiplexing scheme employing FWM is demonstrated in Figure 2.6 where OTDM signal and the clock (i.e. gating) signal at the different wavelength and at the bit rate of a single channel, are propagated through a nonlinear medium. When 1 bit of a single channel overlaps with the clock signal, generated FWM idler (Figure 2.7), which is the exact replica of that channel, is extracted through filtering and it contains demultiplexed data signal from that channel.

FWM process brings two important aspects into demutliplexing techniques. Due to its instantaneous nature, it is suitable for demultiplexing of very high data bit rate signals as well as for generating appropriate gating signals discussed next.

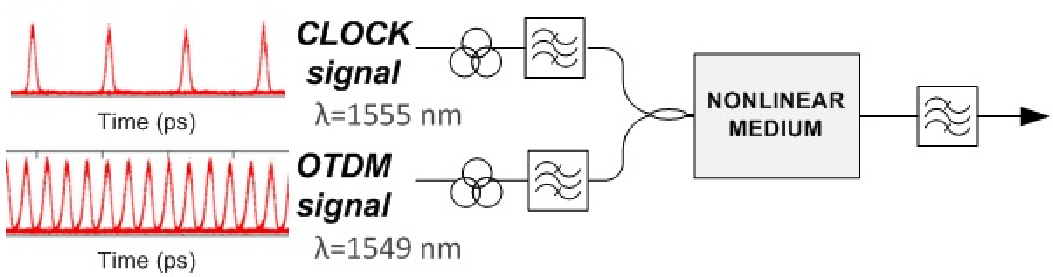

Fig. 2.6 Demultiplexing scheme for OTDM signals based on FWM in a nonlinear medium.

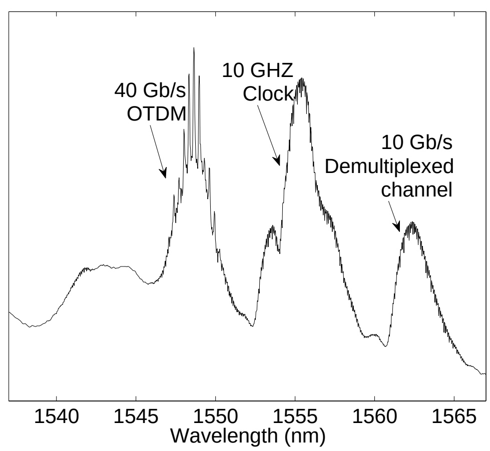

Fig. 2.7 Spectrum of the OTDM signal, clock (gating) signal and a demultiplexed channel.

2.4 Generation of Tunable Optical Delay Lines Through FWM

Implementing all-optical tunable delays has been done through use of slow light schemes using stimulated scattering phenomena (Brillouin and Raman scattering in fibers) [27].

These approaches however have limited achievable delays and limited bandwidth, suffer signal degradation and are not suitable to operate with phase-modulated signals [28]. Another technique for implementing all-optical tunable delays has been demonstrated through wavelength conversion-dispersion principle. The delay is generated as a result of wavelength dependent characteristics of dispersive media. It is represented as a product of dispersion parameter and the amount of wavelength shift. Depending on the response of the chosen medium, the signal is converted to the appropriate wavelength before propagating through and acquiring the desirable delay [28]. Due to its nature, this approach is able to produce large tunable delays and is also transparent to modulation techniques.

Conversion-dispersion based tunable delays can be implemented with many different configurations having in mind that wavelength conversion can be achieved through self phase modulation (SPM), XPM or FWM process and that the dispersive medium can be different fiber based or on-chip devices. All-optical tunable delay used in this thesis is based on FWM process and FBG, and thus is further explained.

Figure 2.8 demonstrates the tunable delay line achieved through wavelength conversion followed by dispersion. A HNLF is used for wavelength conversion via FWM. Two signals are allowed to propagate and undergo FWM process generating the idler. This wavelength converted idler is then coupled to a chirped FBG as a dispersive medium (Figure 2.9). By tuning the pump wavelength and thus shifting the idler, reflected signals can be continuously delayed noting that the achievable delay is the product of the dispersion parameter and the amount of wavelength shift.

2.5 Semiconductor Based OTDM Demultiplexing

2.5.1 OTDM Demultiplexing in SOA and EAM

FWM in fibers and semiconductor optical amplifiers (SOA) for the purpose of OTDM demultiplexing has been investigated since 1991 [21]. When short intense optical pulse is injected into SOA, dynamic change in optical gain and refractive index occurs; injected signal modulates the gain and the refractive index making the medium highly nonlinear. If OTDM signal and the high power clock signal, used as a pump, are propagated through such a medium, FWM occurs and all-optical demultiplexing can be achieved. SOA based demultiplexing schemes employing FWM report demultiplexing of up to 200 Gb/s signal

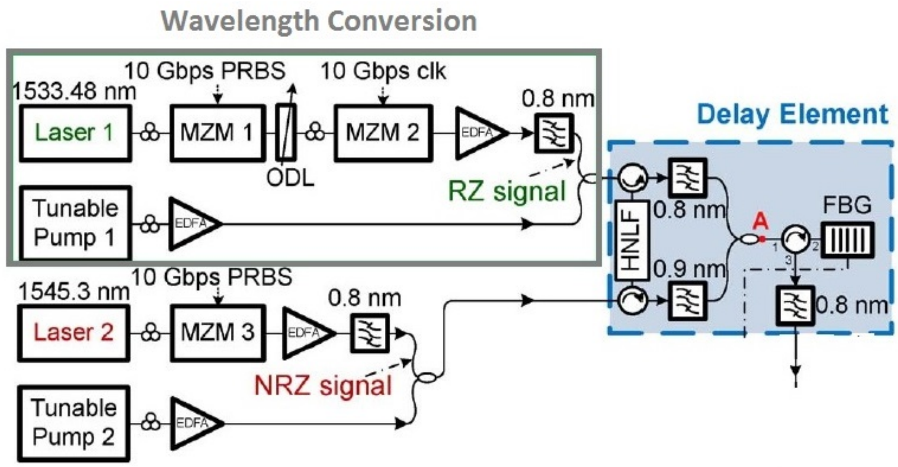

Fig. 2.8 Part of a dual-channel delay experimental setup; demonstration of counterpropagating signals through HNLF. All-optical tunable delay line is demonstrated with wavelength conversion followed by a delay element [28]. © 2009 IEEE

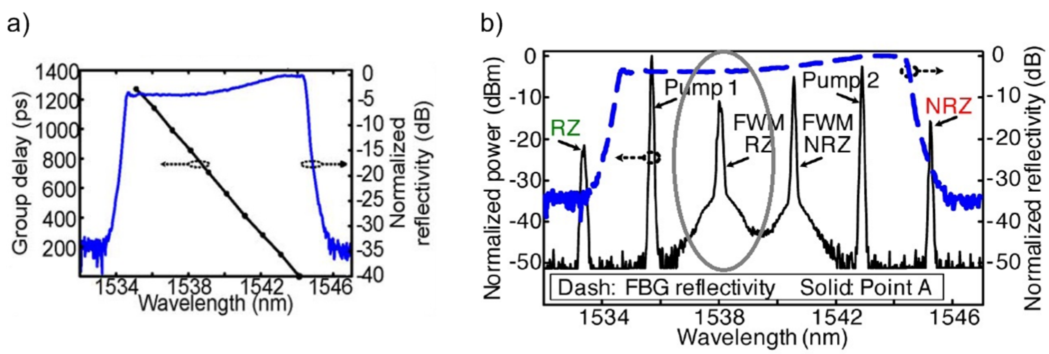

Fig. 2.9 (a) FBG spectrum (b) spectrum of the coupled signals indicating the FWM idler for one of the counterpropagating signals [28]. © 2009 IEEE

(32 × 6.3 Gb/s) and 160 Gb/s signal (4 × 40 Gb/s) in [29]. This technique is also demonstrated on planar lightwave circuit (PLC) integrating optical time division multiplexing and demultiplexing on one chip (Figure 2.10). The FWM of the SOAs is employed to demultiplex 160 Gb/s signal to 8 × 20 Gb/s channels [30]. Compactness, stability and low switching power are the properties that made SOA an attractive device for OTDM systems, however its operating speed is limited by the slow gain recovery time (around 100 ps) preventing it to operate for higher data rates. A great deal of research has been done on improving this time and below 1 ps recovery time is reported in [31], where 40 Gb/s

channels were retrieved from 640 Gb/s signal.

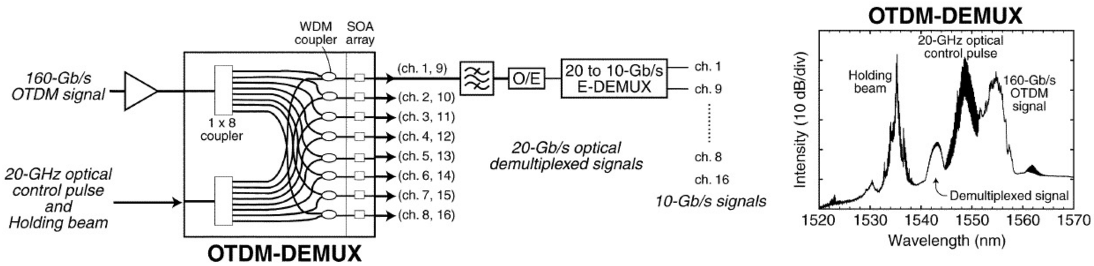

Fig. 2.10 A 160-to-20 Gb/s demultiplexing setup implemented in PLC and its spectrum [30]. © 2004 IEEE

Semiconductor based OTDM demultiplexing has also been demonstrated in EAMs. In this device, an electrical signal controls the switching speed of the modulator that is used to transmit and demultiplex channels. Using EAM is the simplest form of demultiplexing but becomes limited with the speed of electronics. In [32] 160-to-10 Gb/s demutliplexing was reported with 7 dB to 10 dB BER power penalties for different channels. In [33] an EAM was monolithically integrated with a photodiode directly driving the EAM in order to overcome the inherent limitations and avoid the need for the electrical amplifiers. It successfully demonstrated demultiplexing of the signal up to a data rate of 320 Gb/s.

In general semiconductor based switches operate well at data rates up to 160 Gb/s [34]. To reach higher data rates further more complex integration in devices are often needed.

2.6 Fiber Based OTDM Demultiplexing

2.6.1 OTDM Demultiplexing in HNLF

Fiber based nonlinear medium characterized by instantaneous nature of the nonlinear effects, has an advantage over SOA for much faster dynamic response, around a few femtoseconds, making it suitable for high speed switching and ultrafast signal processing. However, typical nonlinear fibers demonstrate low nonlinearity coefficient (γ =2 -10 $W^{-1}km^{-1}$). To achieve high bit rates and high conversion efficiency in such fibers, long fiber lengths are needed (i.e. hundreds of meters). Many nonlinear fibers are therefore altered to increase their nonlinearity and reduce the length to make them more compact: the amount of doping can be increased along with reducing the core diameter; air holes can be introduced into cladding structure creating photonic crystal fibers; different materials with larger nonlinear coefficient can be used instead of silica (i.e. chalcogenides, bismuth oxide) [35].

In [36] 80 Gb/s-to-10 Gb/s demultiplexing was reported through use of 100 m long HNLF and with less than 3 dB power penalty at BER at 10^{-9}. A highly chirped rectangular shaped supercontinuum (SC) source was combined with 80 Gb/s time multiplexed signal in a HNLF. Eight WDM channels with 10 Gb/s wavelength converted signals were extracted simultaneously with each one of them converted to a different centre wavelength. In [37] a photonic crystal fiber with lengths of 50 m and 100 m was used to demultiplex 80 Gb/s-to-10 Gb/s signal with less than 4.6 dB power penalty. The nonlinearity coefficient of this fiber was 11 $W^{-1}km^{-1}$ allowing shorter fiber lengths. In [38] one meter long bismuth-oxide-based fiber was used for demultiplexing of 160 Gb/s-to-10 Gb/s signal. Significantly higher nonlinear coefficient of 1,250 $W^{-1}km^{-1}$ allowed for such a short length. Error free BER was achieved as well, with around 2 dB power penalty. Recently, [39] demonstrated simultaneous demultiplexing of 16 WDM channels in 160 Gb/s-to-10 Gb/s OTDM system (Figure 2.11). A 30 m long HNLF with 11 $W^{-1}km^{-1}$ nonlinear coefficient was used. Power penalty varied among the channels reaching as high as 12 dB.

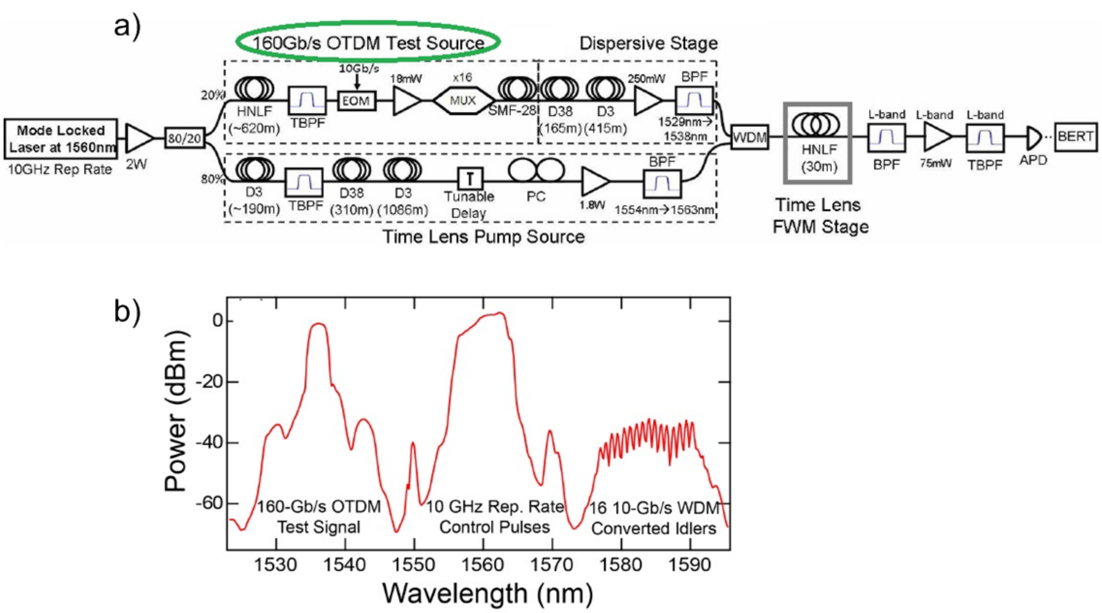

Fig. 2.11 (a) Experimental setup used for simultaneous demultiplexing of all 16 WDM channels from 160 Gb/s OTDM test source (b) the full spectrum after FWM stage for all 16 channels [39].

2.6.2 OTDM Demultiplexing in NOLM

The OTDM demultiplexing implemented in nonlinear optical loop mirror is often based on XPM in HNLF inside the mirror. Figure 2.12 (a) demonstrates the principle of a NOLM configured as a Sagnac interferometer with both ends of the fiber forming a loop connected to a 3 dB coupler. The clock signal that is previously being extracted from the transmitter through a clock recovery scheme, and at the bit rate of a single channel, is injected into the loop to propagate in a clockwise direction. The OTDM signal enters the loop through a 3 dB coupler where it is split into counter propagating signals. Demultiplexing occurs due to XPM taking place in HNLF inside the loop when the clock signal introduces a phase shift onto the specific channel of OTDM signal. The individual channels are often selected using a tunable optical delay line (Δt). However, if several NOLMs are placed in parallel, all channels can be demultiplexed simultaneously [40]. Figure 2.12 (b) demonstrates the optical spectra of the OTDM, clock and demultiplexed signals.

OTDM demultiplexing with NOLMs has been successfully demonstrated since as early as 1993 when 6.3 Gb/s channels were demultiplexed from a 100 Gb/s OTDM signal. Since then the bit rates and the bandwidths expanded. In 2002, 10 Gb/s channels were demultiplexed from 320 Gb/s signal in 100 m long NOLM composed of highly nonlinear dispersion-shifted fiber [42], and by 2009, 1.28 Tb/s signal was successfully demultiplexed to 128 $\times$ 10 Gb/s channels [43]. In 2010, 5.1 Tb/s data signal generated by using 1.28 Tbaud OTDM, DQPSK data-modulation (Figure 2.12), was successfully demultiplexed to 10 Gbaud DQPSK channels [41].

2.7 OTDM Demultiplexing in Nanophotonic Waveguide Devices

Reducing the fiber length to even 1 m as it was demonstrated in [37] still presents a challenge if scaling OTDM systems down to a chip size. SOAs and EAMs are compact and integrable, but cannot achieve fast switching that is possible in HNLF and NOLMs. Nanophotonics gives a new approach to increasing switching speeds and also reducing operating power requirements, through exploiting materials' nonlinearities. Very small waveguide effective area (A_{eff}) directly affects the nonlinear coefficient (γ) making it suitable for ultrafast switching.

In [44] a 5 cm long low-loss chalcogenide glass, As_2S_3, planar waveguide was used for

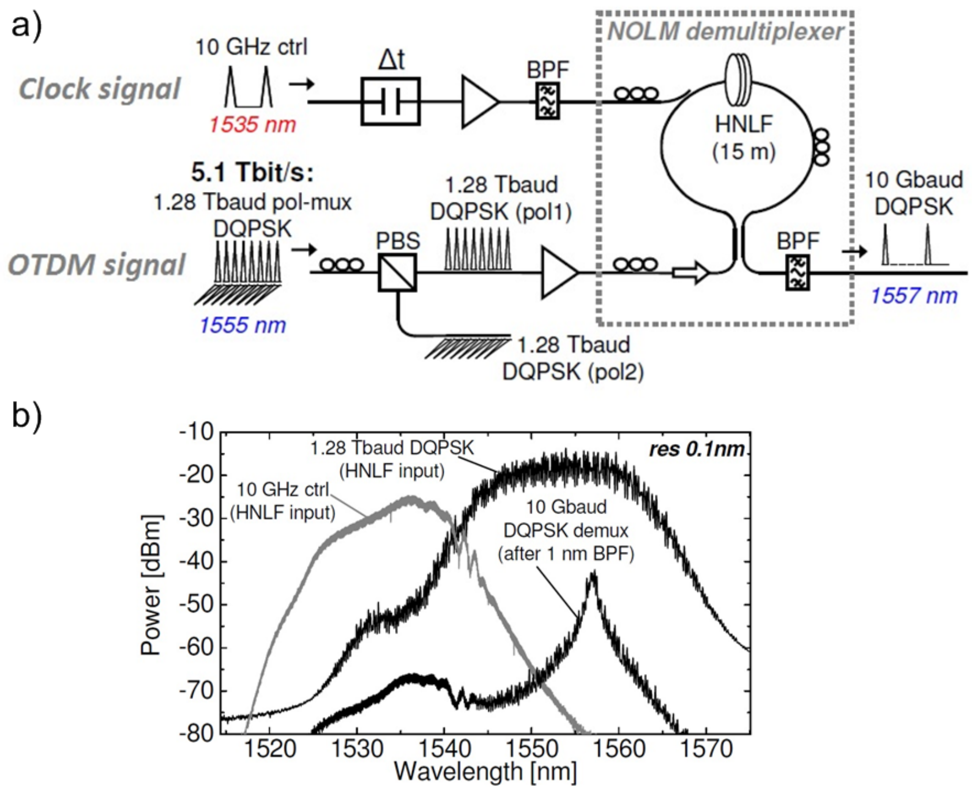

Fig. 2.12 (a) Demultiplexing scheme for OTDM signals based on XPM in a nonlinear optical loop mirror (b) optical spectra, measured in the NOLM demultiplexer [41].

160 Gb/s-to-10 Gb/s demultiplexing with small power penalty of less than 1 dB. The optical waveguide is 3.8 μm wide rib waveguide that is etched 1.2 μm deep in a 2.5 μm thick film of the chalcogenide, deposited on silica-silicon substrate. The waveguide exhibits very high nonlinearity coefficient of 2,080 $W^{-1}km^{-1}$ at 1550 nm.

The same data rate was achieved with a shorter silicon nanowire, being 1.1 cm in length, in [45]. A 160 Gb/s-to-10 Gb/s demultiplexing was performed with $2^{31} - 1$ PRBS signal via FWM on a 450 nm wide and 260 nm thick silicon nanowire on top of 2 μm silicon oxide layer, fabricated through electron beam lithography. Error free operation was achieved with less than 4 dB power penalty.

A 640 Gb/s-to-10 Gb/s and 1.28 Tb/s-to-10 Gb/s error free demultiplexing was demonstrated in a 5 mm long silicon waveguide in [46] (Figure 2.13). The waveguide was fabricated through electron beam lithography on a 300 nm silicon layer on top of 1 μm silicon oxide. The waveguide width was designed for 450 nm with tapered couplers of 40 nm width. Both demultiplexed signals were error free with around 2 dB and 7 dB power penalties respectively.

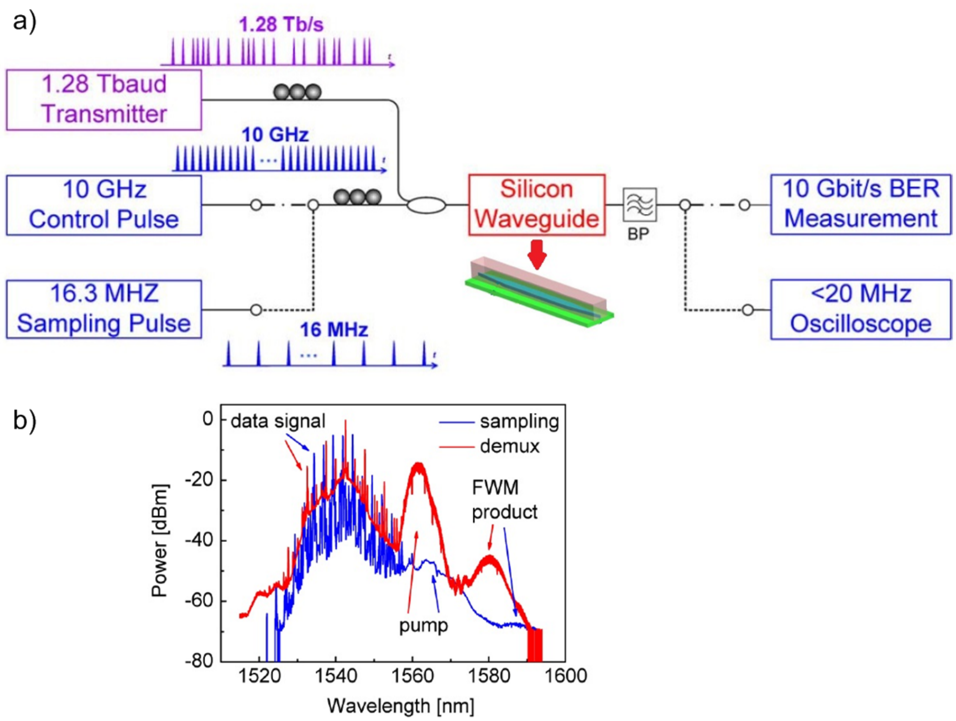

Fig. 2.13 (a) Experimental scheme for serial data signal demultiplexing in silicon waveguide (b) output spectra from the nanoengineered silicon waveguide when performing demultiplexing from 640-to-10 Gb/s [46]. © 2011 IEEE

2.8 OTDM Demultiplexing Techniques Summary

Thus far, various techniques used for all-optical OTDM demultiplexing were presented. Table 2.1 summarizes the reported results when implementing some of the techniques. It highlights the devices being used along with the nonlinear phenomenon and the achieved data bit rates. As previously mentioned, semiconductor based devices lag in the switching speeds when compared to the fiber based devices due to their inherent properties. Fiber based devices when employed in the form of a NOLM achieve very high data bit rates but are limited in modulation format choice. XPM phenomenon employed in NOLMs prevents any phase modulated schemes. Consequently, FWM process is employed in many schemes as it adds the important advantage of being transparent to modulation formats. HNLFs combined with FWM require great lengths to achieve higher switching speeds and are often altered in their composition to make them more compact. This leads to increased interest in nanophotonic waveguide devices. Silicon waveguides employing FWM process have already demonstrated great potential for high data bit rates (i.e. in [46]) and when combined with their high integrability it becomes an obvious choice for implementing all-optical signal processing schemes.

	Device	Phenomenon	Data bit rate (modulation format)	Year	Ref.
Semiconductor based	SOA	FWM	200 Gb/s-to-6.3 Gb/s (OOK)	1996	29
		FWM	160 Gb/s-to-40 Gb/s (OOK)	2002	29
		FWM	160 Gb/s-to-20 Gb/s (OOK)	2004	30
		XGM	640 Gb/s-to-40 Gb/s (OOK)	2007	31
	EAM	XAM	160 Gb/s-to-10 Gb/s (OOK)	2004	32
		XAM	320 Gb/s-to-10 Gb/s (OOK)	2003	33
Fiber based	HNLF	FWM	80 Gb/s-to-10 Gb/s (OOK)	2001, 2012	35, 36
		FWM	160 Gb/s-to-10 Gb/s (OOK)	2006, 2013	37, 38
	NOLM	XPM	320 Gb/s-to-10 Gb/s (OOK)	2002	41
		XPM	1.28 Tb/s-to-10 Gb/s (OOK)	2009	42
		XPM	5.1 Tb/s: 1.28 Tbaud-to-10 Gbaud (DQPSK)	2010	39
Nanophotonic waveguides	As_2S_3	FWM	160 Gb/s-to-10 Gb/s (OOK)	2007	43
	silicon nanowire	FWM	160 Gb/s-to-10 Gb/s (OOK)	2010	44
	silicon waveguide	FWM	640 Gb/s-to-10 Gb/s (OOK)	2011	45
		FWM	1.28 Tb/s-to-10Gb/s (OOK)	2011	45

Table 2.1 Summarized techniques used for all-optical OTDM demultiplexing. XGM: cross gain modulation, XAM: cross absorption modulation, As_2S_3: chalcogenide glass planar waveguide.

Chapter 3

Experimental FWM Based OTDM Demultiplexing Using SOI

3.1 Previously Achieved Results Using HNLF with Bidirectional Propagation

As described in chapter 2, FWM is an instantaneous nonlinear process that can be effectively used for OTDM demultiplexing and implementing optical tunable delay lines through wavelength conversion followed by dispersion. Many different configurations can be employed for realizing these two processes through FWM and chapter 2 lists some of the most common ones. The importance of a reduced size and compactness along with high data rates further motivates configurations that would have the minimum component count. In [28] it is demonstrated how a single piece of HNLF can be used bidirectionally to implement both the tunable optical delay and the demultiplexing process without introducing crosstalk in between counterpropagating signals. This is a promising concept as the two processes can potentially be implemented in a nanosize waveguide instead of a bulky HNLF. Additionally, dispersion based delay device can also be implemented in nanophotonic structures potentially yielding fully integrated OTDM demultiplexer.

This thesis is heavily based on the experiment and results demonstrated in [47]. A 40 Gb/s PRBS signal is demultiplexed error free with a 10 GHz gating signal. Both gating signal generation and demultiplexing process are performed through FWM in a single HNLF that is used bidirectionally with intentions to reduce the component count. The gating signal is generated with a conversion-dispersion principle. Figure 3.1 shows the setup used in this experiment.

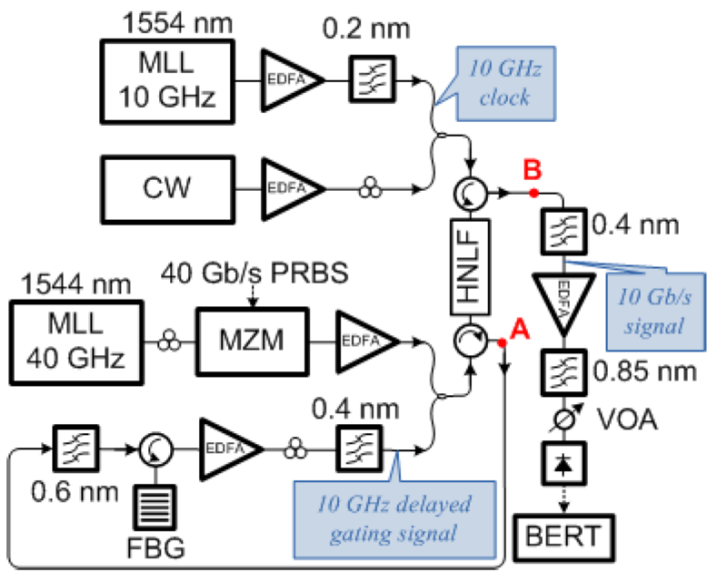

Fig. 3.1 Experimental setup; MLL: Mode-locked laser, MZM: Mach Zehnder modulator, EDFA: Erbium doped fiber amplifier, VOA: Variable optical attenuator, BERT: Bit error rate tester, FBG: Fiber Bragg grating [47].

Mode-locked laser (MLL), outputting pulses at 10 GHz repetition rate, and continuous wave (CW) signals are both amplified to around 10 dBm and 12 dBm power levels respectively, before they are allowed to propagate through 1 km long HNLF. The fiber has the nonlinear coefficient of 10 $W^{-1}km^{-1}$ and is designed for zero dispersion around 1554 nm with a dispersion slope of 0.02 ps/(nm^2·km). The two signals undergo FWM and thus generate 10 GHz gating signal that is wavelength converted from the MLL. In order to time align this gating signal for the demultiplexing process, a dispersive medium, chirped fiber Bragg grating (FBG), is used. FBG has 48.7 ps/nm dispersion and its group delay response is shown in Figure 3.2. The signal acquires different delays depending on the wavelength being reflected. For demultiplexing a 40 Gb/s signal every channel is 25 ps apart and with the given FBG response, wavelengths in steps of 0.51 nm result in time displacements steps of 25 ps. Given this, MLL pulse train is locked to 1554 nm wavelength, while the CW is tuned from 1555.7 nm to 1557.23 nm in order to produce the idler at the specific wavelengths that will acquire the desired delay in FBG.

A second MLL is operating at the 40 GHz repetition rate, and is intensity modulated by

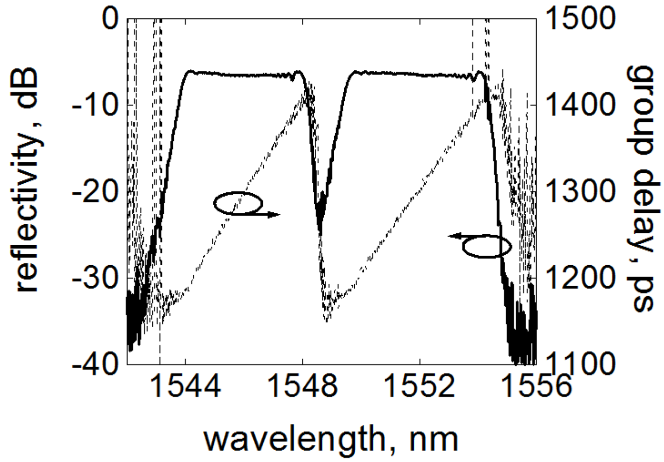

Fig. 3.2 FBG group delay response.

Mach-Zehnder modulator generating return to zero (RZ) signal containing $2^{31}-1$ pseudo random binary sequence (PRBS) data. This signal mimics the OTDM signal containing 4×10 Gb/s channels and is locked to 1544 nm wavelength. Gating signal and OTDM signals are then sent through HNLF where 4 channels are demultiplexed one by one by filtering the respective FWM idlers.

Bit error rate measurements were reported, however they could not be compared to the back to back measurement as 40 Gb/s data was not a true time multiplexed signal. The measurements still confirmed error free operation (Figure 3.3). Four demultiplexed channels that are 25 ps apart are shown in Figure 3.4.

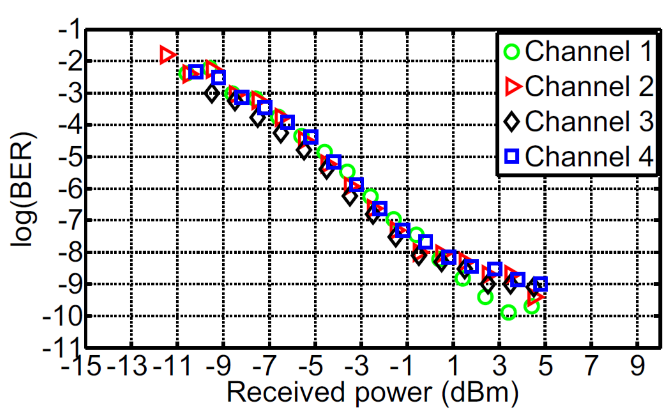

Fig. 3.3 Bit error rate measurements for the four demultiplexed channels at 10 Gb/s [47].

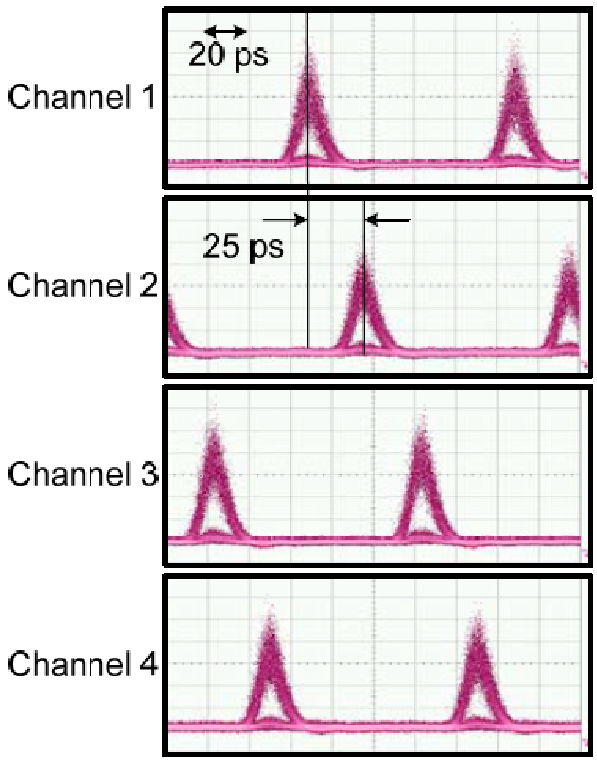

Fig. 3.4 The oscilloscope trace of the 10 Gb/s demultiplexed signals [47].

3.2 Demonstration of the Results of FWM Conversion Efficiency in Silicon Waveguides

In work to be described in this thesis, OTDM demultiplexing of 40 Gb/s-to-10 Gb/s data is achieved through use of silicon waveguides. The detailed analysis of the performance of the waveguides had to be done prior to demultiplexing experiment.

Silicon waveguides were designed by Jia Li[1] as part of Silicon Nanophotonics Fabrication course in 2011. The incentive was to design the waveguides suitable for nonlinear processes, in particular FWM, with close to zero anomalous dispersion around 1550 nm. The waveguides were fabricated through IMEC's Multi-project Wafer Shuttle run[2] in 220 nm thick

[1] A PhD candidate at McGill, supervised by professor Lawrence R. Chen.

[2] IMEC is a micro and nanoelectronics research center in Belgium that offers fabrication of passive and active nanophotonic devices on silicon wafers through Multi-project Wafer Shuttle (MPW) runs. MPW is a process in which designs of several users are combined on the same wafer thus reducing the individual cost of fabrication per user.

silicon layer on top of 2 μm silicon oxide on silicon wafers (Figure 3.5). The process offered an additional top oxide cladding as well as full etching through 220 nm or half etching through 70 nm. Ten different configurations in terms of waveguide width, waveguide length, with top oxide or air cladding were fabricated in order to achieve the best FWM conversion efficiency. The configurations are the combinations of two different waveguide widths (650 nm and 500 nm), with 5 different waveguide lengths (28 mm, 20 mm, 12 mm, 7 mm and 4 mm), with air cladding and with top oxide cladding (Figure 3.6). A few replicas of the same devices were fabricated on different places on the silicon wafer to account for the fabrication variability and were compared to each other. The waveguides were characterized based on the coupling and propagation loss, two-photon absorption and free carrier effect induced nonlinear propagation loss, and FWM conversion efficiency.

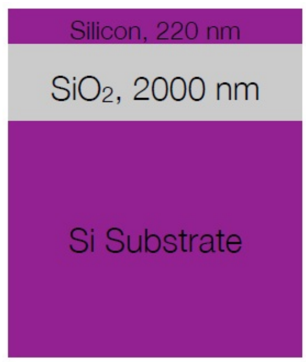

Fig. 3.5 Silicon on insulator cross section.

Fig. 3.6 Silicon waveguides layout.

Access to the waveguides is through one dimensional grating couplers optimized for vertical coupling (Figure 3.7). The couplers are designed by IMEC and optimized for TE polarization only. They are designed for theoretical 31% coupling efficiency which corresponds to 5.1 dB coupling loss, and 40 nm 1 dB bandwidth. The optimum coupling is achieved with near vertical fiber placement, around 10 degrees from the vertical axis.

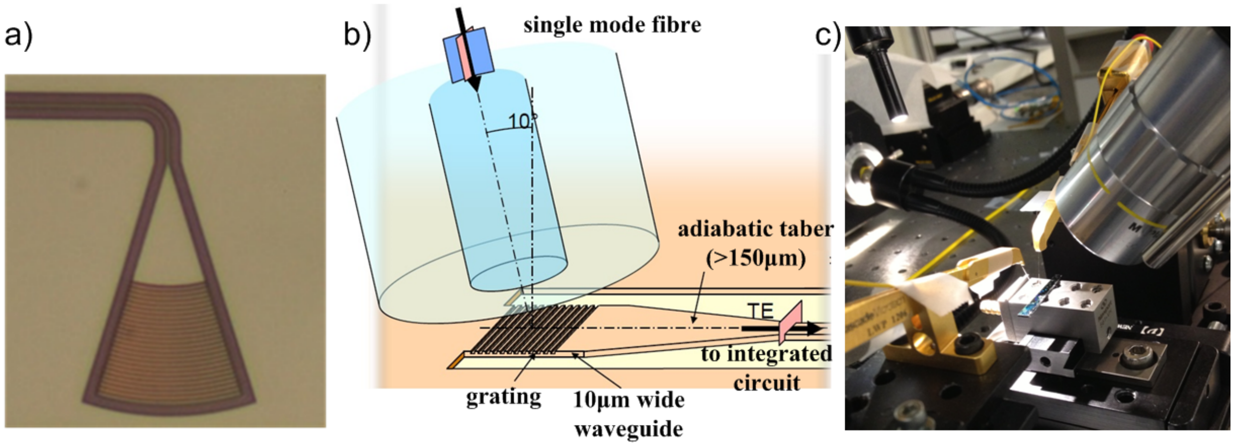

Fig. 3.7 (a) IMEC's grating coupler layout (b) fiber and coupler optimum alignment (from the course notes of EECE 584 CMC-UBC Silicon Nanophotonic Fabrication Course) (c) experimental setup showing the probes used for coupling light into the chip.

When testing for the coupling and the propagation loss, a broadband source was used for characterization and it was coupled into the waveguides through polarization controller in order to select TE polarization only (Figure 3.8). The results were recorded using Optical Spectrum Analyzer (OSA). Figure 3.9 shows that wavelength dependent loss is present and it comes mainly from the grating couplers, but it still allows for a wide wavelength range to be used for practical experiments (1520 nm -1560 nm). Measurements on around 15 different devices were recorded and experimental coupling loss was averaged to around 9.3 dB per coupler for waveguides with air cladding, and around 7.5 dB per coupler for waveguides with top oxide. Propagation loss was calculated to be around 2.4 dB/cm and around 1.5 dB/cm, respectively for the two cases. The coupling losses are higher compared to the theoretical value (5.1 dB) which is mainly attributed to the angle setting of the coupling fiber with respect to the grating coupler. Achieving optimum angle can be further optimized with rotation stages permitting precise angle adjustment which were not used in the current setup. Additionally, polarization fluctuation induced input loss can also be taken into account as the input fiber was non polarization-maintaining.

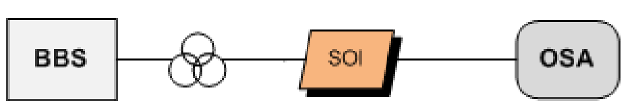

Fig. 3.8 Experimental setup for characterizing losses in silicon waveguides.

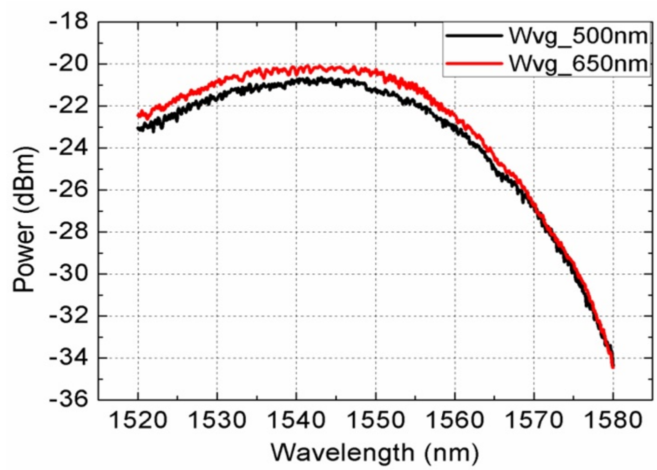

Fig. 3.9 Wavelength dependent loss (measured and recorded by Jia Li).

The waveguides were designed for nonlinear processes that often require high input powers, therefore, they were also characterized for two-photon absorption and free carrier effect induced propagation loss. A CW signal was being amplified before propagating through the waveguide (Figure 3.10) and the power of the signal was measured at the input and at the output of the chip with the two power meters. The output power level as a function of the input power level is shown in Figure 3.11. The measured results (red curve) were plotted against the ideal case (black curve) that takes into account the coupling and linear propagation loss only. From the figure, it was noted that two-photon absorption and free carrier effect induced nonlinear propagation loss is negligible for the input powers below 100 mW. However, as the input power increases, the nonlinear loss is taking effect. For instance, when the input power was 400 mW the nonlinear loss was around 2 dB. The waveguides were not tested for higher input powers as it was observed that the grating couplers could be damaged when the input power is larger than 500 mW.

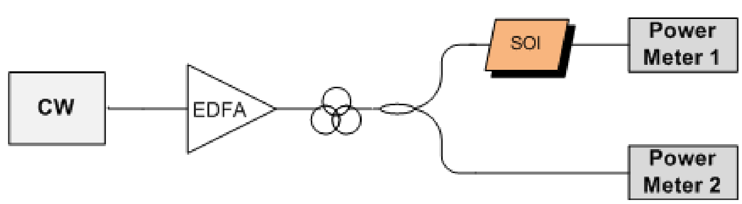

Fig. 3.10 Experimental setup for characterizing two-photon absorption and free carrier effect induced nonlinear propagation loss in silicon waveguides.

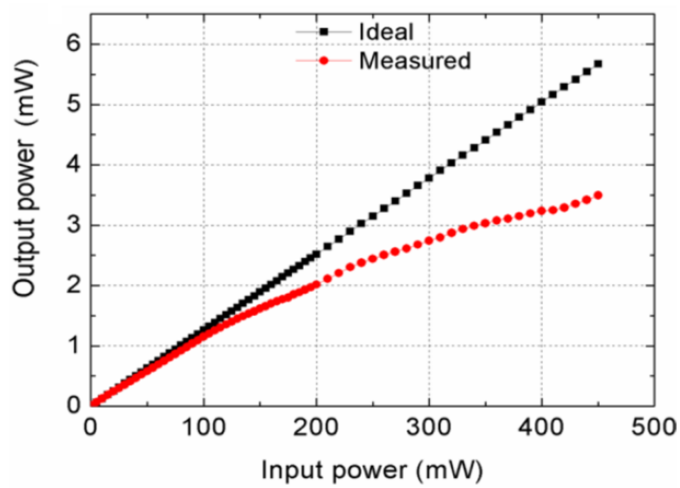

Fig. 3.11 Two-photon absorption and free carrier effect induced nonlinear propagation loss in silicon waveguides.

Silicon waveguides were also tested for FWM conversion efficiency. For the degenerate case of FWM, the conversion efficiency is defined through comparative power levels of idler and signal $CE = P_{idler}/P_{signal}$. For characterizing the devices, two CW signals were amplified and launched into the silicon waveguides (Figure 3.12). The state of the polarization was adjusted using two polarization controllers. The optical power and spectrum were recorded in a power meter and the OSA. The efficiency was measured against the signal wavelength detuning from the pump, against the pump power and against the length of the waveguides. For conversion efficiency versus wavelength detuning (Figure 3.13 (a)) the pump wavelength was set to 1545 nm with the power of 250 mW. The probe wavelength was initially set to 1543 nm with the power of 12 mW. The trace shows small variations in conversion efficiency. The difference between the highest and the lowest recorded values is 2.4 dB across 10 nm range. This suggests that FWM 3 dB bandwidth is at least 10 nm wide which is broad enough for most applications. For conversion efficiency versus the pump power (Figure 3.13 (b)), the pump and the signal were kept at the same initial wavelengths as for the previous measurement. The power of the pump was varied from 100 mW to 450 mW with 50 mW steps. The trace shows the gradual decrease in the efficiency with the decrease in the pump power which is expected. For conversion efficiency versus waveguide length (Figure 3.13 (c)), the pump and the signal were kept the same as before with pump being around 250 mW, and they were propagated trough different waveguides.

Longer waveguides show better efficiency for FWM.

Based on the collected results better conversion efficiency is achieved in waveguides with top oxide and 12 mm to 28 mm in length, with the pump power of around 200 mW and higher. However, beyond 200 mW two-photon absorption and free carrier effect induced nonlinear propagation loss takes effect introducing additional losses.

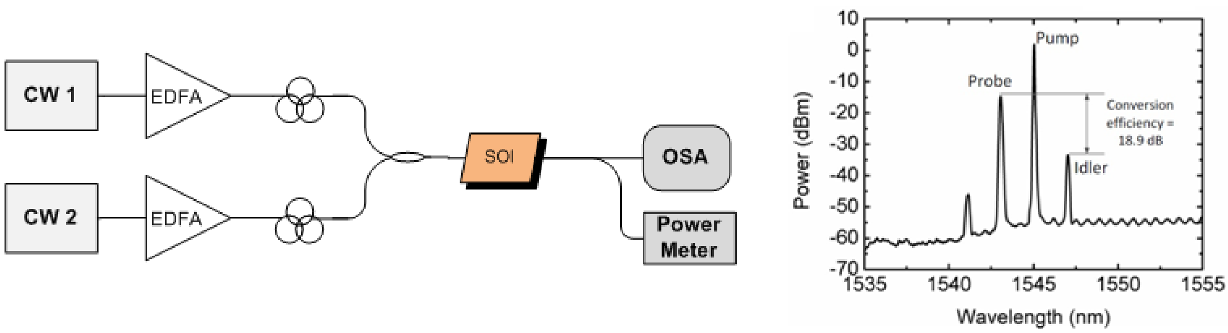

Fig. 3.12 Experimental setup for characterizing FWM conversion efficiency in silicon waveguides with the sample spectrum of FWM in silicon waveguide (measured and recorded by Jia Li).

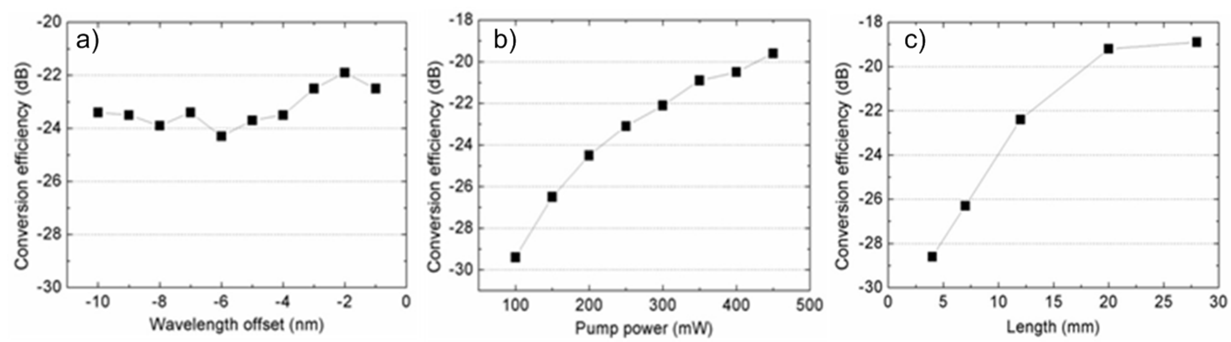

Fig. 3.13 FWM conversion efficiency (a) versus wavelength detuning from the pump (b) versus pump power (c) versus waveguides length (measured and recorded by Jia Li).

3.3 OTDM Demultiplexing in SOI

OTDM demultiplexing of 40 Gb/s-to-10 Gb/s data achieved through use of silicon waveguides is presented here. The experimental setup consists of two stages, generating the gating signal or optical tunable delay stage, and demultiplexing of OTDM channels. Both gating signal and the 40 Gb/s OTDM signal that is to be demultiplexed are generated from the same 10 GHz laser source. The waveguide used for both applications is with top oxide, 12 mm in length and 650 nm in width. Longer waveguides were not used because they were demonstrating an increase in overall insertion loss. Despite the best achievable coupling loss in the waveguides with top oxide of 7.5 dB per coupler, the average fiber to fiber loss achieved would be around 20 dB or more when performing experiments requiring a lot of equipment and for extended time period. This is most likely due to high activity around the coupling stages affecting the alignment of the fibers with the grating couplers as well as affecting the final polarization before coupling in. Overcoming such high losses required much of optimization in the setup in terms of the equipment choice and its arrangement as well as the wavelength choice. The two experimental stages were intended to be implemented bidirectionally through a single waveguide, as in [47]. However, additional circulators that would be needed for bidirectional propagation were introducing extra loss that proved to significantly reduce the signal-to-noise ratio of the gating signals, thus affecting the performance of demultiplexing process. Hence, in the second stage of the experiment silicon waveguide was replaced with HNLF when generating the delay line.

3.3.1 OTDM Demultiplexing in SOI: Stage 1 - Demonstration of the Results from Tunable Optical Delay with SOI and FBG

Generation of gating signals was implemented in a continuously tunable optical delay line based on a conversion-dispersion principle described in section 2.4. FWM process was employed and the same FBG device that was characterized in section 3.1.

Figure 3.14 shows the experimental setup used. Two signals, a pulse train and a continuous wave, are propagated through silicon waveguide where they undergo FWM resulting in wavelength conversion of the 10 GHz pulse train in form of generated idler. The idler is then propagated in FBG in order to acquire desired time delay for the demultiplexing process.

Before choosing any of the parameters a few limiting factors had to be taken into account. Knowing that FWM conversion efficiency would average to around -23 dB (refer to Figure 3.13) in addition to around 20 dB coupling loss into the chip, extracting the idler with sufficient signal-to-noise ratio presented a challenge. For that reason, FWM idlers

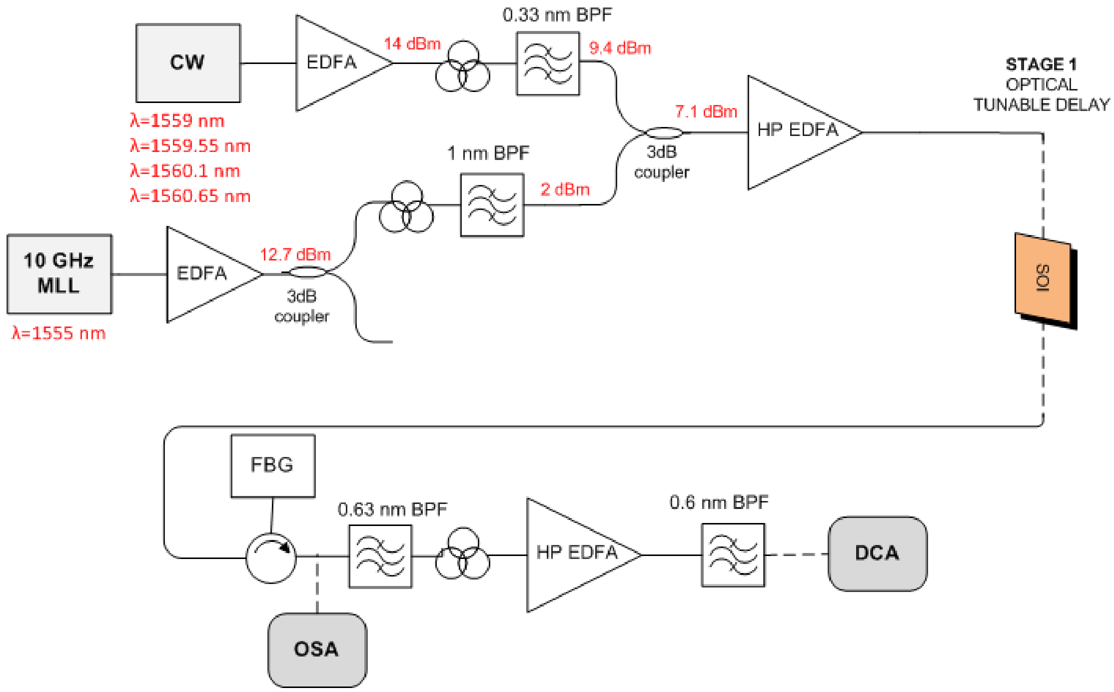

Fig. 3.14 Experimental setup for gating signal generation (i.e. tunable optical delay line) in silicon waveguide.

were generated such that they occur in the peak of the grating coupler bandwidth (1540 nm -1550 nm) (refer to Figure 3.9). They also had to correspond with the FBG spectral response, meaning they had to occur in its linear regime, from 1548 nm and toward shorter or from 1549 nm and toward longer wavelengths (refer to Figure 3.2). Pulse train from mode lock semiconductor laser (MLL) was tuned to 1555 nm, while continuous wave (CW) was tuned from 1559 nm to 1560.65 nm, generating FWM idlers at 1551 nm, 1550.45 nm, 1549.9 nm and 1549.35 nm. As explained in section 3.1, these exact wavelength steps of 0.51 nm would, after propagating in FBG, result in time displacement steps of 25 ps which corresponds to the bit windows associated with the 40 Gb/s signal operation.

To compensate for the coupling losses and to facilitate the FWM process that is power and polarization sensitive, many amplifiers had to be employed. Many filters were consequently used to reduce ASE noise from the amplifiers. Thus, both MLL and CW signals were amplified and then filtered. CW signal was amplified originally to 14 dBm and filtered with a narrow 0.33 nm bandwidth bandpass filter (BPF) having 5.6 dB insertion loss. The MLL generates around 2.2 ps long pulses with a 100 ps period (Figure 3.15 (a)), resulting in short duty cycle and high peak powers. The rms timing jitter is around 440 fs. The pulse signal was originally amplified to 12.7 dBm average power and split with 3 dB coupler to be used for gating signal generation and 40 Gb/s OTDM data signal generation. The ASE noise was then filtered with 1 nm bandwidth BPF having 2.5 dB insertion loss. The 3 dB bandwidth of the original 10 Gb/s signal is around 1.5 nm (Figure 3.15 (b)). With 1 nm BPF the signal duration becomes around 8 ps, resulting in around 13 dBm peak power. The two signals are again amplified with high power amplifier providing up to 30 dB gain before they are propagated through the silicon waveguide. After FWM process, the idlers are extracted with 0.63 nm BPF before they are amplified to desired power levels for demultiplexing process. To improve their signal-to-noise ratio even further, ASE noise is filtered after amplification with another 0.6 nm BPF. Figure 3.15 (c) shows FWM occurring for 4 different CW signals generating 4 different idlers that are propagated in FBG. The traces of 4 different gating signals obtained through this process are shown in the Figure 3.15 (d). The pulsewidth of the signal is influenced by the last 0.6 nm BPF and it is around 13.3 ps with rms timing jitter ranging from 1.7 ps to 3.8 ps for different traces.

All the spectral measurements were collected with the OSA with 0.06 nm resolution bandwidth and -60 dBm sensitivity level. The time domain measurements were collected with the digital communication analyzer (DCA) having the optical sampling module with 65 GHz bandwidth corresponding to 7.6 ps impulse response. The electrical trigger used for DCA is a precision time base trigger with persistence time of around 300 ms and the rms timing jitter noise floor of 200 fs.

3.3.2 OTDM Demultiplexing in SOI: Stage 2 - Demonstration of the Results from Demultiplexing in SOI

The demultiplexing part of the experiment was implemented employing FWM process in a silicon waveguide. Figure 3.16 shows the experimental setup. The gating signal generation was performed in HNLF instead of inside the waveguide, as explained earlier. The setup was then simplified further by bypassing the FBG and delaying the gating signal with the optical tunable delay line (OTDL) instead. This was done to avoid wavelength tuning of multiple filters following the grating.

The MLL outputting pulse trains as 10 GHz repetition rate at 12.7 dBm average power was split with 3 dB coupler to be used for gating signal generation and 40 Gb/s OTDM

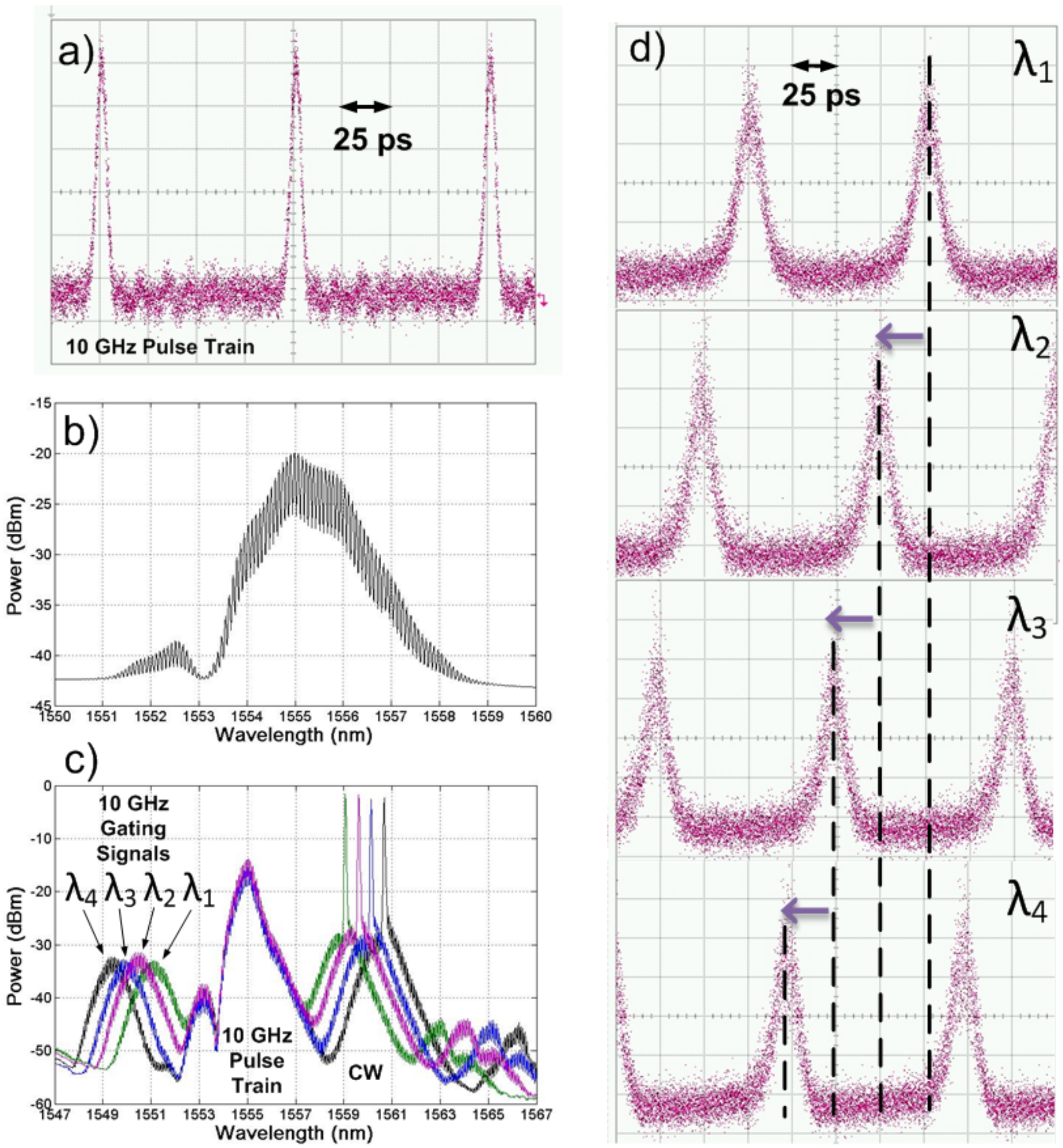

Fig. 3.15 (a) time and (b) spectral response of the 10 GHz mode locked laser (c) FWM in between MLL and CW signals and the corresponding idlers (d) four gating signals 25 ps apart for demultiplexing 4 OTDM channels.

data signal generation. Multiplexing was achieved in the optical multiplexer (OMUX). The 40 Gb/s OTDM signal can be generated by using two of the four independent stages available in the unit. If 10 Gb/s input signal is modulated with a $2^7 - 1$ PRBS pattern, the multiplexer ensures a true $2^7 - 1$ PRBS pattern at the output.

After 3 dB coupler, the 10 GHz signal was first attenuated to around 0 dBm average

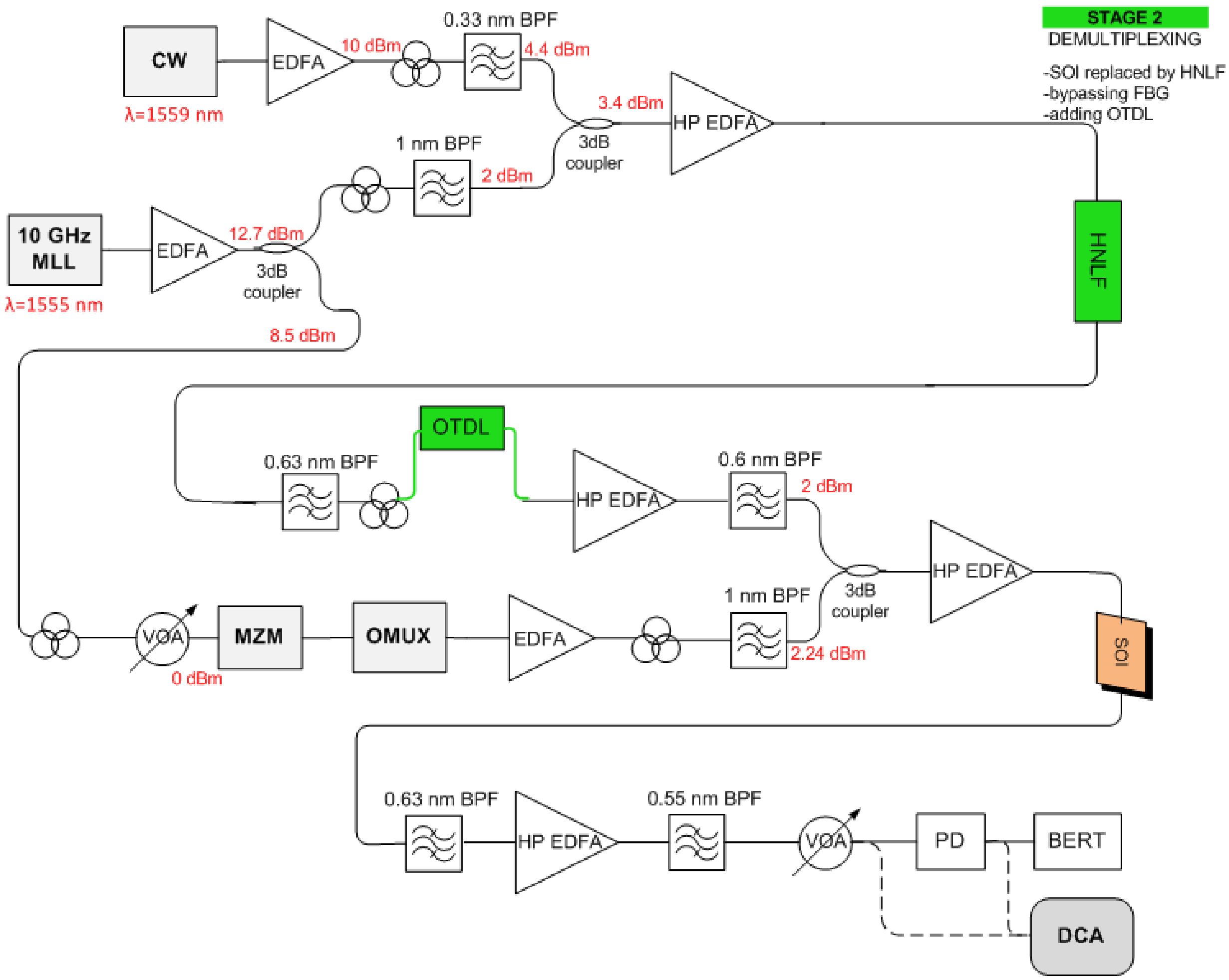

Fig. 3.16 Experimental setup for demultiplexing of 40 Gb/s-to-10Gb/s OTDM signal in silicon waveguide.

power before being modulated with Mach-Zehnder modulator generating RZ-IM signal containing $2^7 - 1$ PRBS data. A 10 Gb/s PRBS data was optically multiplexed to 40 Gb/s PRBS data through OMUX before being amplified to a desired power level for FWM and filtered with 1 nm BPF. The pulsewidth of the 40 Gb/s data is around 8 ps resulting in around 7.2 dBm peak power.

Gating signal is generated with the same 10 GHz laser tuned to 1555 nm and CW laser tuned to 1559 nm. CW signal is amplified to 10 dBm and both signals are provided around 11 dB gain through the amplifier, before propagating through HNLF, which is less gain than in the case with SOI as there is no need to compensate for the coupling loss.

HNLF dispersion is zero around 1554 nm with a dispersion slope of 0.02 ps/(nm^2·km) with nonlinear coefficient of 10 W^{-1}km^{-1}. FWM idler, at 1551 nm wavelength (Figure 3.17 (a)), is filtered and amplified as in the previous case, except that CW signal is not tuned through different wavelengths to generate different idlers, but OTDL is used to manually delay the 10 GHz gating signal in 25 ps steps. The pulsewidth of the idler is around 13.3 ps resulting in 10.8 dBm peak power.

The two signals, 10 GHz FWM idler and 40 Gb/s data signal, are provided around 18 dB gain before propagating through silicon waveguide and undergoing FWM (Figure 3.17 (b)). The idler representing demultiplexed channel is extracted with 0.63 nm BPF before being detected for the bit error rate measurements. Figure 3.17 (c), (d) shows 40 Gb/s PRBS data after OMUX and a single 10 Gb/s demultiplexed channel after begin detected with a photodiode. Bit error rate measurements were collected with a DC-to-12 GHz photoreceiver having 0.6 A/W responsivity.

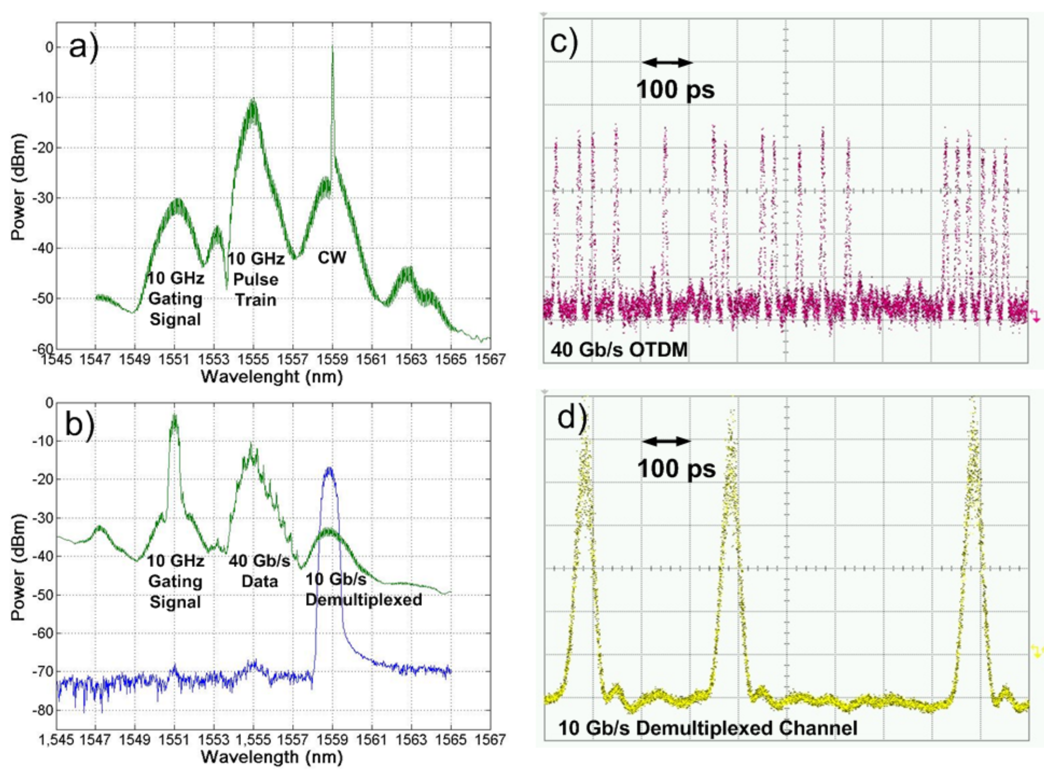

Fig. 3.17 (a) gating signal generation in HNLF (b) demultiplexing of one of the channels in SOI (c) 40 Gb/s PRBS data signal before being demultiplexed (d) 10 Gb/s demultiplexed channel.

Four channels are demultiplexed individually and their corresponding traces in both optical and electrical domain are shown in Figure 3.18. All of the channels demonstrate open eyes. Furthermore, bit error rate measurements indicating error free operation for BER at 10^{-9} are shown in Figure 3.19. Significant power penalty of 6.5 dB to 7 dB is recorded. The back-to-back measurement is recorded after MZM followed by 1 nm BPF resulting in a pulse that is around 8 ps in duration. For the demultiplexing process through the FWM many EDFAs are employed to compensate for lossy coupling into silicon waveguide while adding significant ASE to signals. Consequently, the demultiplexed channels acquire noise through the process along with their longer duration after 0.55 nm BPF (i.e. around 15 ps) which could contribute to the penalty.

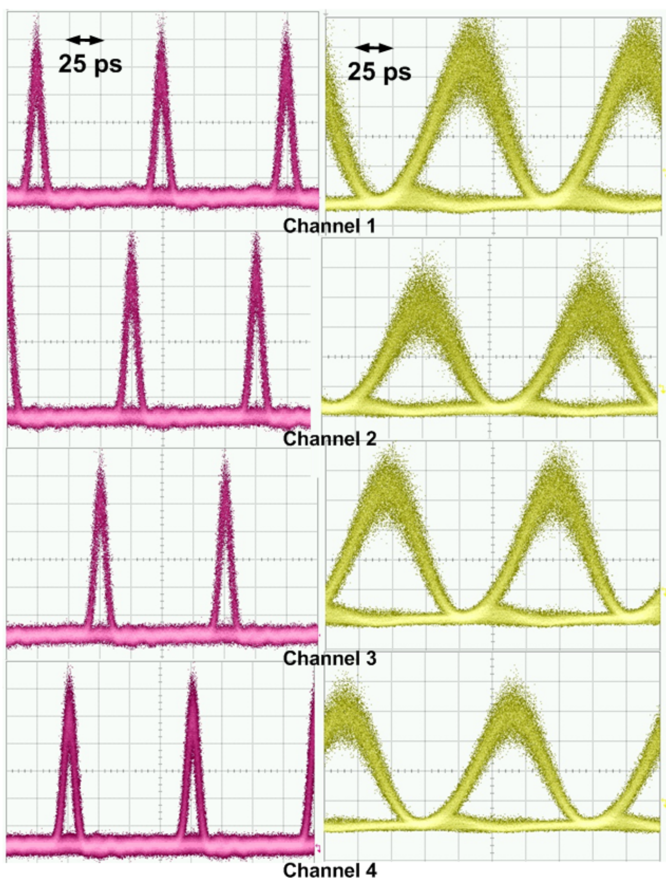

Fig. 3.18 Four demultiplexed channels and their corresponding traces in both optical and electrical domain.

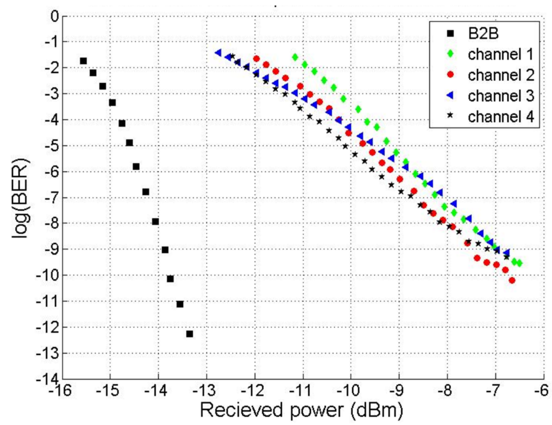

Fig. 3.19 Bit error rate measurement for the back-to-back and for the four demultiplexed channels at 10 Gb/s.

3.4 OTDM Demultiplexing in SOI Summary

Chapter 3 demonstrates a successful OTDM data signal demultiplexing process of 40 Gb/s-to-10 Gb/s data signal. The process employs generation of continuously tunable delay line prior to demultiplexing operation both implemented in silicon waveguides and both exploiting FWM phenomenon. Tunable optical delay line is based on conversion-dispersion principle accomplished with FWM and FBG structure. It demonstrates continuous tunability across the selected wavelength range and generation of four gating signals in between 1549 nm and 1551 nm and with 1.7 ps to 3.8 ps timing jitters for different signals. All the gating signals demonstrate sufficient signal-to-noise ratio required for further demultiplexing operation. The OTDM demultiplexing is based on FWM phenomenon used for channel extraction accomplished through gating signal alignment with the selected timing window. It demonstrates 4 error free demultiplexed channels with around 7 dB power penalty.

The experiment is conducted in two separate stages due to high coupling loss of the silicon waveguides. However, it clearly demonstrates how tunable delay line followed by demultiplexing operation can be accomplished in silicon waveguide through bidirectional propagation if these losses are reduced. This would yield to full OTDM demultiplexing with reduced component count in nanosize medium. The experiment also demonstrates the potential for scalability to higher data bit rates (i.e. 160 Gb/s) and different modulation formats (i.e. DPSK, DQPSK) as it relies on FWM that is ultra-fast and phase preserving process.

Chapter 4

Design and Preliminary Results on Step-Chirped and Serial Gratings in SOI

Bragg gratings developed to be one of the most widely employed devices in communication networks for its versatile applications in routing, filtering, dispersion compensation, optical delays, fiber based amplifiers, lasers, etc [48]. Their implementation has been accomplished in both fiber and nanophotonic devices for supporting a wide range of requirements in mentioned applications. With significant focus toward a size reduction and integration of optical components, research in waveguide gratings has been drawing increasing attention.

4.1 Bragg Gratings Background

The electric field propagating through a medium is characterized by its propagation constant (β) and the effective refractive index (n) of that medium where both can be modulated in a controlled way to predict the characteristics of the electric field [49].

The wave equation describing unperturbed field modes is

$$\nabla^2 \mathbf{E}(\mathbf{r}, t) - \mu_0 \varepsilon(\mathbf{r}) \frac{\partial^2 \mathbf{E}}{\partial t^2} = 0 \tag{4.1}$$

ε is electric permittivity of the medium, and μ_0 is magnetic permeability of free space. If polarization of the medium is altered in any way, it will deviate from that which accompanies the unperturbed mode and the wave equation will become

$$\nabla^2 \mathbf{E}(\mathbf{r},t) - \mu_0 \varepsilon(\mathbf{r}) \frac{\partial^2 \mathbf{E}}{\partial t^2} = \mu_0 \frac{\partial^2 \mathbf{P_{pert}}(\mathbf{r},t)}{\partial t^2} \tag{4.2}$$

where $\mathbf{P_{pert}}(\mathbf{r},t)$ is a distributed polarization source. By altering the medium, perturbation can be introduced and one way is by a distributed feedback structure (Figure 4.1) formed by physical corrugation of the interface (Λ is the grating period). In this case perturbation is defined as

$$\mathbf{P_{pert}}(\mathbf{r},t) = \varepsilon_0 \Delta n^2(\mathbf{r}) \mathbf{E}(\mathbf{r},t) \tag{4.3}$$

where Δn represents the refractive index modulation. In order to solve this modified wave equation accounting for introduced perturbation two assumptions can be made: electric field is polarized in y-direction only and coupling from guided to radiation modes can be ignored. For the case of the distributed feedback structure, the field can propagate in forward and the backward direction (Figure 4.1) forming counterpropagating waves. Total electric field for all the propagating modes can then be expanded to

$$E_y(\mathbf{r},t) = \frac{1}{2} \sum_m A_m(z) E_y^m(x) e^{j(\omega t - \beta_m z)} \tag{4.4}$$

where A_m is the amplitude of the m^{th} mode. Substituting equation (4.4) and (4.3) into the wave equation yields complex modified wave equation. In order to solve it, additional assumptions can be made. The refractive index modulation (Δn) can be assumed to be sinusoidal and the higher order terms in Fourier series expansion of the perturbation can be ignored. This significantly simplifies defining the counterpropagating waves and coupling in between them. The modified wave equation can then be solved through a set of master coupled mode equations [50]

$$\begin{aligned} \frac{dA_m^-}{dz} &= K A_m^+ e^{-j2\Delta\beta z} \\ \frac{dA_m^+}{dz} &= K^* A_m^- e^{j2\Delta\beta z} \end{aligned} \tag{4.5}$$

where $A_{+/-}^m$ represents the amplitude of the m^{th} mode in forward and backward direction respectively, K is the coupling coefficient and $\Delta\beta$ is detuning from the propagation constant. Coupling coefficient and detuning can be defined as

$$K = \frac{\pi \Delta n}{\lambda}\eta \tag{4.6}$$

$$\Delta\beta = \beta - \frac{\pi}{\Lambda} = \frac{2n_{ave}\pi}{\lambda} - \frac{\pi}{\Lambda} \tag{4.7}$$

where η is the overlap factor, n_{ave} is the average refractive index. As previously mentioned, radiation modes can be ignored and only a discrete number of modes will be guided. Therefore, it can be assumed that coupling between forward and backward propagating waves will only occur if they are in phase, satisfying the relations $\beta_0 = \frac{\pi}{\Lambda}$ and $\Lambda = \frac{\lambda}{2n_{ave}}$. Hence, the characteristics of the propagating field are affected by the refractive index that can be altered by changing the period of the grating.

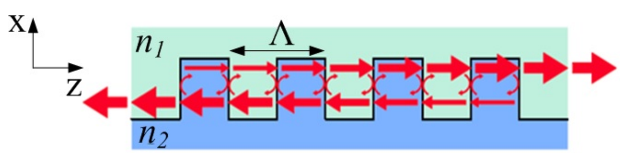

Fig. 4.1 Distributed feedback structure showing coupling of power between counter propagating modes/waves (modified from the course notes of ECSE 527 Nonlinear Optics taught at McGill).

To fully resolve forward and backward propagating modes the set of master coupled equations can be analyzed with Transfer Matrix Method (TMM) as shown.

$$\begin{vmatrix} a(0) \\ b(0) \end{vmatrix} = \begin{vmatrix} T_{11} & T_{12} \\ T_{21} & T_{22} \end{vmatrix} \begin{vmatrix} a(L) \\ b(L) \end{vmatrix} \tag{4.8}$$

$$a(z) = A_m^+(z)e^{j\beta z}$$

$$b(z) = A_m^- e^{-j\beta z} \tag{4.9}$$

$$T_{11} = T_{22}^* = \frac{\Delta\beta \sinh(\gamma L) + j\gamma \cosh(\gamma L)}{j\gamma} e^{-j\beta_0 L} \tag{4.10}$$

$$T_{12} = T_{21}^* = \frac{K \sinh(\gamma L)}{j\gamma} e^{j\beta_0 L} \tag{4.11}$$

$$\gamma = \sqrt{K^2 - \Delta\beta^2} \tag{4.12}$$

The grating can be designed to fully reflect a wave propagating with a particular wavelength while transmitting everything else, acting as a wavelength selective reflection filter. The equations (4.10) and (4.11) can then be used to calculate the reflection (r) and the transmission (t) coefficients and determine the reflectivity (R) (transmissivity (T)) of the grating as follows

$$R(\lambda) = |r(\lambda)|^2 = \left|\frac{T_{12}}{T_{22}}\right|^2 \tag{4.13}$$

$$T(\lambda) = |t(\lambda)|^2 = \left|\frac{1}{T_{22}}\right|^2 \tag{4.14}$$

If the grating period is to be nonuniform, in particular linearly chirped (Figure 4.2 (a)), the reflection spectrum broadens and wider span of propagating wavelengths gets reflected by the grating while also introducing group delay that is linearly changing with respect to the wavelength (Figure 4.3). This particular property can be used for optically delaying the signal with respect to wavelength. Group delay can analytically be approximated by differentiating the phase of the reflection coefficient with respect to frequency.

The principle behind achieving linearly chirped period is to split a grating of length L into M sections, where each section is of length δl having a uniform period Λ_m ($1 < m < M$) that differs from the previous one by a certain increment value ($\delta\Lambda$) defining the change in the period [48] (Figure 4.2 (b)).

$$\Lambda_m = \Lambda_{m-1} + \delta\Lambda \tag{4.15}$$

$$\delta\Lambda = \frac{\Delta\Lambda\delta l}{L} \tag{4.16}$$

where $\Delta\Lambda$ is the total chirp of the grating. If $\delta\Lambda$ and the sections are sufficiently small, the grating becomes continuously linearly chirped. Otherwise, the gratings are referred to as step-chirped. The important parameters to choose become the number of sections and their length. The lengths of the subsections end up being only approximately the same, as there has to be an integer number of periods in each subsection to avoid any phase mismatch. The concept of step-chirped gratings and their fabrication was introduced in 1994 in [51].

4.2 Gratings Implementation: FBG versus SOI Grating

Fiber Bragg gratings were first demonstrated by Hill et al. [53] and became popular for its low insertion loss, polarization independence, wide tunability in spectral characteristics and eventually well-established fabrication technology. Conventional way to form fiber gratings

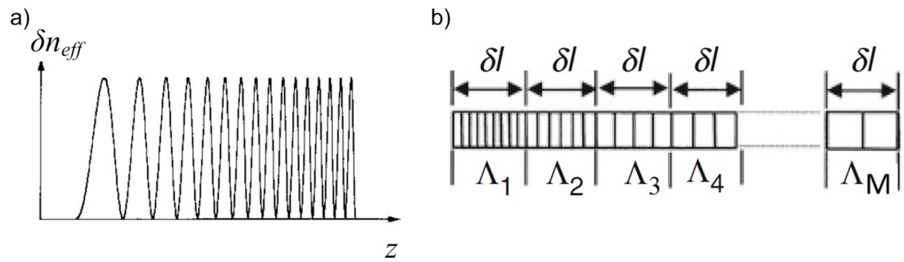

Fig. 4.2 (a) Linearly chirped refractive index profile [52] (b) the step-chirped phase mask [48].

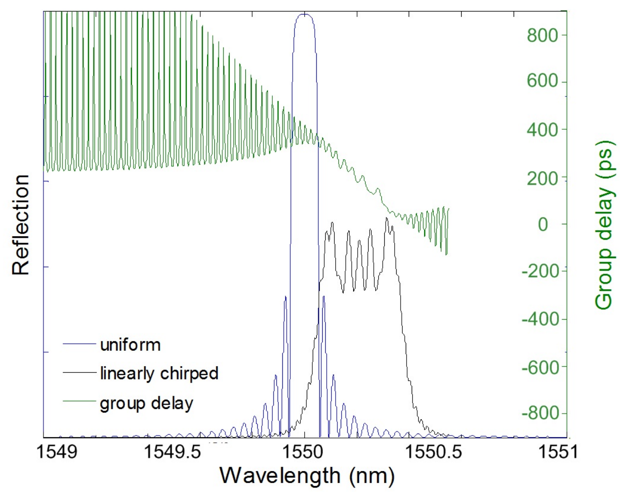

Fig. 4.3 Reflection and group delay response of a fiber Bragg grating: $\Delta n = 8 \times 10^{-5}$, $\delta\Lambda = 0.7 \times 10^{-14}\ m^2/m$, $L = 2\ cm$ (simulated in MATLAB).

is by UV exposure through a phase mask to produce periodic index modulation [48, 54]. Advances in technology development gave rise to various designs of fiber gratings allowing well controlled amplitude and phase responses through different index modulation schemes: uniform, chirped, apodized, phase-shifted, sampled, etc. However, all fiber based schemes suffer from bulkiness and low time resolution; lengths of centimeters became common to achieve the desired peak reflectivities over wide bandwidths. With developing silicon photonic integration on-chip gratings started drawing more attention for their reduced size, improved time resolution and higher coupling coefficient that is achieved in silicon waveguides (i.e. coupling coefficient of around 10 cm^{-1} in fiber versus 70 cm^{-1} in waveguides [55]).

Work described here focuses on optical delays achieved in integrated gratings. Tunable optical delay devices have already been successfully implemented using slow light elements and fiber or waveguide gratings [27]. Silicon on insulator based delay lines have been realized using tapered gratings [56], tapered sidewalls [57], and chirped sidewall grating structures [58] (Figure 4.4), as well as through coupled ring resonator structures [59]. Devices to be described explore the effects of sidewall grating structures through serial sidewall Bragg grating arrays and the step-chirped sidewall Bragg gratings. Intended fabrication process allowed for two fixed top-etched depths thus sidewall grating structure was considered and implemented as it provided more freedom in design process. The achieved results require further optimization in order to be comparable to the properties of the FBG used in the demultiplexing experiment. Nevertheless, SOI gratings still promise advantages over the fiber based devices for its size and relatively simple fabrication approach.

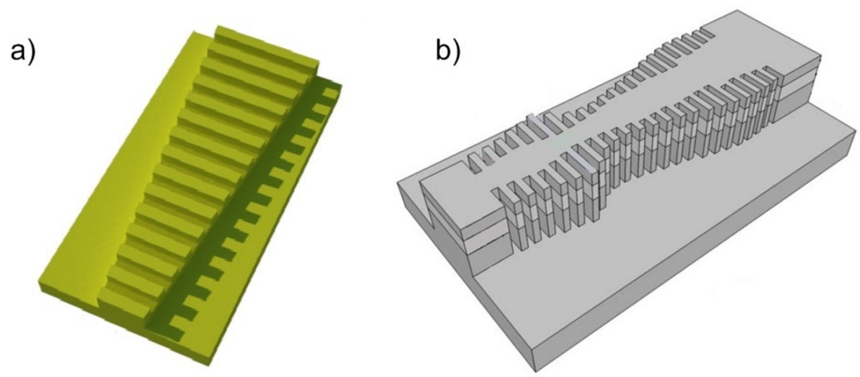

Fig. 4.4 (a) top-etched tapered gratings [56] (b) chirped sidewall gratings [55].

4.3 Design and Fabrication Parameters

Silicon Bragg waveguides were designed as part of the Silicon Nanophotonics Fabrication course in 2012. The devices were fabricated through electron beam lithography at the University of Washington Microfabrication/Nanotechnology User Facility[1]. The gratings were fabricated on a 220 nm thick silicon layer on top of 2 μm silicon oxide on silicon wafers with both full (220 nm) and half (70 nm) etching possibilities and with 2, 4 and 6 nm fabrication grids. The incentive was to design the step-chirped gratings that could introduce the delays in steps of 25 ps so that FBG used in OTDM demultiplexing experiment can be

[1]Member of the NSF National Nanotechnology Infrastructure Network

replaced with the silicon Bragg gratings that could be integrated with previously designed silicon waveguides.

Several parameters come to affect the response of the grating and its group delay. The widths W_1 and W_2 (Figure 4.5) determine the number of modes supported and the respective effective refractive indices. Corresponding refractive indices determine the coupling coefficient between forward and backward propagating waves (refer to equation (4.6)). The difference between the widths, the corrugation depth $\Delta W = \frac{W_1 - W_2}{2}$, also affects the coupling coefficient as well as the strength of reflectivity and spectral response bandwidth. The period Λ determines the frequency response and the delay and it is given by $\Lambda(z) = \Lambda_0 + \frac{\Delta\Lambda}{L} z$ for any point z across the grating length L; $\Lambda_0 = \frac{\lambda_B}{2n_{ave}}$ is the average period with λ_B being the Bragg wavelength, and $\Delta\Lambda$ is the total chirp in the grating period. Term $\frac{\Delta\Lambda}{L} z$ represents the increment step size for the changing grating period. The smaller this term is the more toward linearly changing chirp regime the design approaches. The term represents the main limiting factor in achieving desired time and spectral response as it is guided by the grid resolution of the fabrication technology. If the grating length is divided into M segments for which the grating period is changing, then the single segment at any point z can be expressed as $z = \frac{L}{M}$. Linearly changing period becomes $\Lambda(z) = \Lambda_0 + \frac{\Delta\Lambda}{M}$ where $\frac{\Delta\Lambda}{M}$ term represents the increment step for the grating period. Figure 4.6 shows the relation between the number of segments, the total chirp and increment step. For 2, 4 and 6 nm steps that were available for fabrication, a few different configurations could be used.

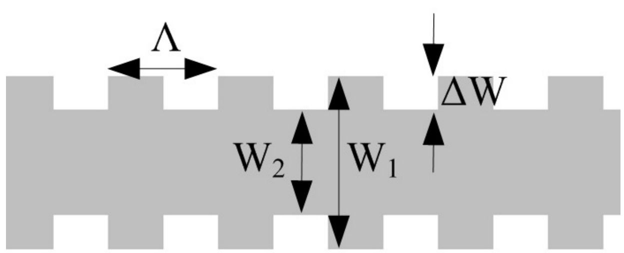

Fig. 4.5 Horizontal cross section of the grating.

The height of the waveguide was chosen to be a standard 220 nm height provided by fabrication specifications. From previous research [60] for the waveguide of 220 nm height to operate in single mode the width needs to be around 440 nm. Above that the waveguide starts supporting a second TE-like mode where above 660 nm width it supports a second TM-like mode as well. Based on this data the waveguide width was chosen in the range of

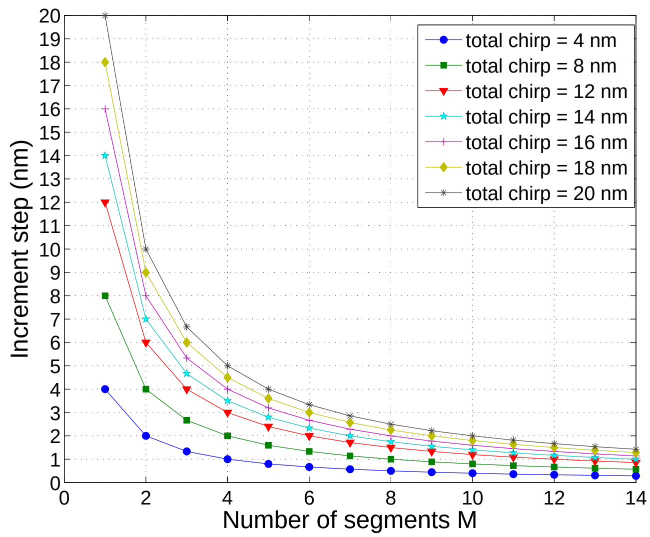

Fig. 4.6 Number of segments versus increment step size.

460 nm and 600 nm.

Various designs with different parameters were simulated in MATLAB using transfer matrix solution to coupled mode equations for spectra and group delay estimation. Multiple assumptions were made to simplify calculations. The effective index method was implemented with eigenmode solver in MODE simulations to approximate the effective indices of strip waveguides with different widths. The average effective index of the grating structure was then calculated for different devices using $n_{ave} = \frac{n_1+n_2}{2}$, where n_1 and n_2 are the indices corresponding to grating widths W_1 and W_2 (Figure 4.5). Since no appodization was implemented, the refractive index modulation Δn was approximated as the difference between the two effective indices $\Delta n = n_1 - n_2$. Spectra and group delays were then estimated with TMM equations introduced in section 4.1. Group delay calculations were also conducted based on the group refractive index extraction from the FDTD simulation taking into account different waveguide widths [60] where the acquired delay can be calculated using $\Delta T = L\frac{n_g}{c}$; L being the distance the wave travels. When estimating the group delay with either method, by differentiating the phase of the reflection coefficient or by extracting the group index, certain assumptions had to be made thus introducing uncertainties. Among others, TMM implemented in MATLAB assumes sinusoidal effective index modulation and coarsely approximates average effective index, while FDTD simulation assumes propagation through a strip waveguide with a constant width.

The two final approaches to realize the group delay through sidewall modulation are presented in Figure 4.7. In Figure 4.7 (a), uniform gratings of different periods are cascaded being physically separated by strip waveguides of a constant length ΔL meant to introduce additional travel time for different resonating wavelengths (i.e. a serial grating array). Two devices, each with five uniform gratings with W_1 width of 500 nm and a sidewall corrugation depth of 20 nm were fabricated with starting grating period $\Lambda_1 = 338$ or 336 nm that is decreasing by 6 or 4 nm respectively, for every successive grating. Each grating comprises 2000 periods resulting in a grating length of ~630 μm; the grating duty cycle is 50%. The gratings are separated by 370 μm strip waveguides such that the center-to-center spacing between gratings is ~1 mm. This is meant to create ~25-28 ps delay (assuming a group index of ~4.2 extracted from FDTD for ~480 nm waveguide width), spanning the bandwidths of 135 and 95 nm, respectively. In the second approach, see Figure 4.7 (b), the physical separation between uniform gratings (ΔL) was reduced essentially to zero, creating a step-chirped sidewall grating structure. In this case, the structures have W_1 waveguide widths of 540, 580 nm and 520 nm with a sidewall corrugation depth of 20 nm. The structures have an overall grating length ~2.8 mm intended to introduce ~20, 15 and 13 ps delay steps, respectively (assuming group index ~4.1-4.2). As previously explained, the limitations of the fabrication grid dictate the increment size to each period as well as the number of segments. This results in devices with 4, 5 or 6 segments, corresponding to starting period of $\Lambda_1 = 304$, 302, or 310 nm, that is increasing by 6, 4 or 2 nm respectively, for every successive grating. Table 4.1 summarizes chosen parameters for 5 different devices.

Parameters	Serial grating array		Step-chirped gratings		
Grid resolution (nm)	4	6	2	4	6
Number of segments, M	5	5	6	5	4
$W1$ (nm)	500	500	520	580	540
Starting period, Λ_1 (nm)	336*	338*	310	302	304

Table 4.1 Parameters of serial array and step-chirped sidewall Bragg gratings: *succeeding periods decrease.

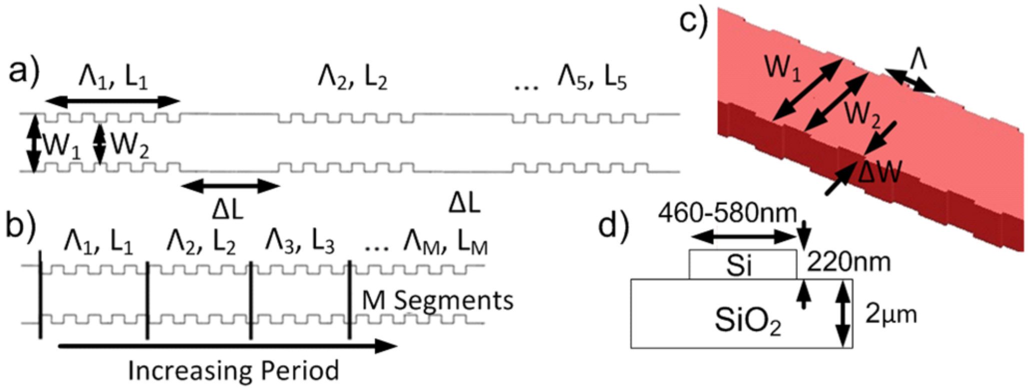

Fig. 4.7 Schematic diagram of fabricated devices (a) serial sidewall Bragg grating arrays showing uniform gratings with different grating periods and strip waveguides separating the gratings (b) step-chirped sidewall Bragg gratings showing grating segments with different grating periods (c), (d) cross sectional view of the waveguide showing important design parameters: waveguide widths (W_1, W_2), corrugation depth (ΔW) and grating period (Λ).

The layout of the designs is shown in Figure 4.8, where same vertical grating couplers are used for input and output coupling as explained in section 3.3. For extracting the reflected signal, an on-chip 1×2 splitter (Y-branch) is used.

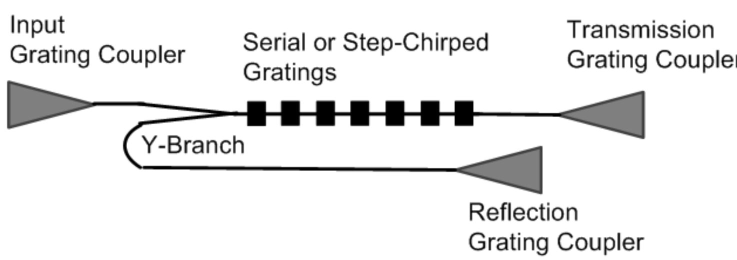

Fig. 4.8 Schematic diagram and layout of devices.

4.4 Experimental Characterization Results

The experimental setup for testing the time domain response of the proposed devices is shown in Figure 4.9. A tunable laser is modulated by a 10 GHz sinusoidal signal and then amplified to compensate for 20-30 dB on-chip losses. This accounts for losses coming from coupling, propagation and 1×2 splitter as well as from slight surface scratches obtained

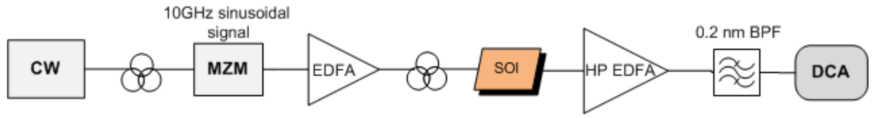

Fig. 4.9 Experimental setup for testing the time domain response of waveguide gratings.

during fabrication process. The output from the tunable laser was tuned to wavelengths within each grating band before allowing it to propagate through the gratings. The output from the waveguide gratings is amplified again and filtered before being detected with an optical sampling module (impulse response of 7.6 ps) connected to a DCA. The operating bandwidth of the C-band EDFAs used to compensate for losses, as well as the range of the tunable laser, limit the number of wavelengths (gratings) used when characterizing time response. The transmission and reflection spectra measurements were recorded at UBC and were constrained to a wavelength of 1570 nm due to limitations of the instruments used. The spectra indicating the wavelengths of the signals (indicated by the arrows) for which the devices were tested and their corresponding delays are shown in Figures 4.10 - 4.11 along with the simulated spectra. Measured spectra are normalized with respect to the grating coupler response. For some devices the spectra span beyond 1570 nm thus the total bandwidth ranges were estimated. Table 4.2 summarizes achieved experimental results compared to the expected simulated values. Spectra responses are simulated with TMM implemented in MATLAB and group delays are calculated based on the group refractive index extraction in FDTD.

	Serial grating array		**Step-chirped gratings**		
Reflection bandwidth or range, [simulated] (nm)	53 [95]	72 [135]	33 [72]	58 [91]	62 [89]
Average delay between adjacent bands, [simulated] (ps)	20 [25]	15 [25]	14 [13]	15 [15]	31 [20]
Total measured delay (ps)	60	29	28	26	63
Total expected delay (ps)	80	60	70	~60	~90

Results

Table 4.2 Results of serial array and step-chirped sidewall Bragg gratings.

Serial sidewall Bragg grating arrays fabricated with 4 and 6 nm grids (Figure 4.10) demonstrate bandwidths of 53 and 72 nm and delays of 20 and 15 ps, respectively. Discrete gratings result in distinct reflection bands (Figure 4.10 (a)), however a quasi-continuous reflection spectrum can be obtained with higher resolution grid, as was anticipated from simulations. Figure 4.10 (b) proves this by showing the bands that slightly overlap. Due to previously mentioned limitations in wavelength range, 4 out of 5 gratings were addressed in 4 nm device resulting in total obtained delay of 60 ps, however a total of ∼80 ps should be achievable. For a 6 nm device, only 3 gratings could be accessed resulting in 29 ps delay, or ∼60 ps total delay if all of the gratings were tested.

Step-chirped sidewall Bragg gratings fabricated with 2, 4 and 6 nm grids (Figure 4.11) demonstrate the bandwidths of 33, 58 and 62 nm which correspond to delays of 14, 15 and 31 ps, respectively. For the highest grid resolution (2 nm), a quasi-continuous reflection spectrum was again obtained while 4 and 6 nm devices demonstrate discrete bands. For 2 nm device, 3 of the 6 available gratings were tested resulting in total obtained delay of 28 ps. A total of ∼70 ps should be achievable if all of the gratings were accessed. For 4 and 6 nm devices, only 3 gratings could be used as well resulting in 26 and 63 ps total obtained delays, or ∼50 and ∼90 ps total delays if all of the gratings were tested.

The spectra results for all of the devices show 30-50% of narrowing in bandwidth compared to the simulations. This is mainly due to small variations in the width of fabricated waveguides as well as the rounding effect of square-corrugation grating profiles [61]. The sidewalls of the waveguides were designed with square modulation mask profile (refer to Figure 4.7) and it has been shown that after electron beam lithography the fabricated gratings become more rounded [61]. In [61], a comparison of measured bandwidth versus design corrugation depth was made for three different modulation mask profiles (square, triangle and sinusoidal) showing that sinusoidal profile approximates the experimental results the best. This effectively means that with the rounding effect, the true corrugation depth becomes smaller than what it is designed for (i.e. 20% smaller in [61]). As the corrugation depth is increasing, the average effective index is decreasing and by Bragg condition ($\lambda_B = 2\Lambda_0 n_{ave}$) this leads to blueshift of the Bragg wavelength. Also, as the corrugation depth is increasing, the coupling coefficient increases which leads to broader spectral bandwidth [62]. With this in mind a simulation fit to the experimental results was demonstrated for two step-chirped sidewall Bragg gratings structures fabricated with 4 nm and 6 nm grid. As the corrugation depth is closely related to the waveguide width, the two

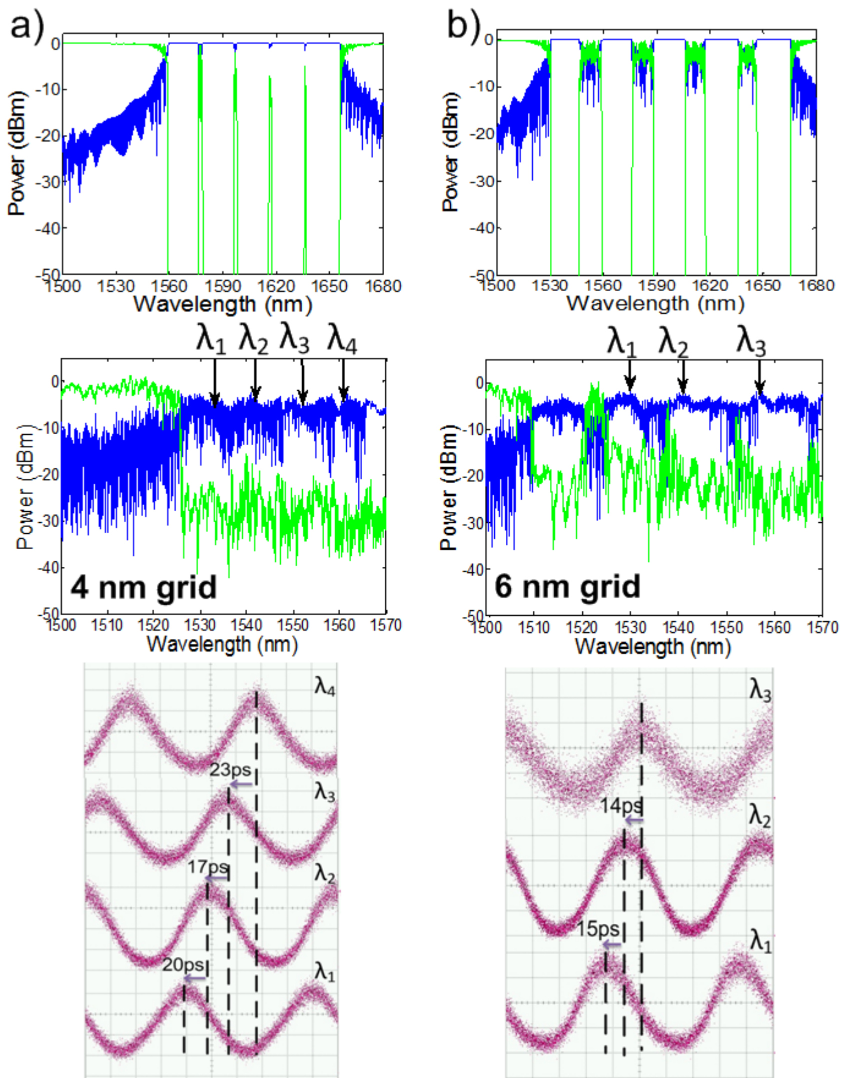

Fig. 4.10 Serial sidewall Bragg grating arrays fabricated with 4 and 6 nm grids with simulated (top) and experimental (bottom) spectra responses and corresponding sinusoidal signals delayed in time (20 ps/div): (a) $W_1 = 500$ nm, $\Delta W = 20$ nm, $\Lambda_1 = 336$ nm. (b) $W_1 = 500$ nm, $\Delta W = 20$ nm, $\Lambda_1 = 338$ nm. Simulations obtained with TMM implemented in MATLAB. Experimental spectra (transmission and reflection) recorded by Valentina Donzella at UBC.

parameters were adjusted. Additionally, increment in grating period was adjusted as well since it is the most affected by the grid resolution. Figure 4.12 shows the comparison to the measured results. For both cases the corrugation depth was decreased by 20%, from 20 nm to 16 nm, while the increment in grating period was reduced from 4 nm to around

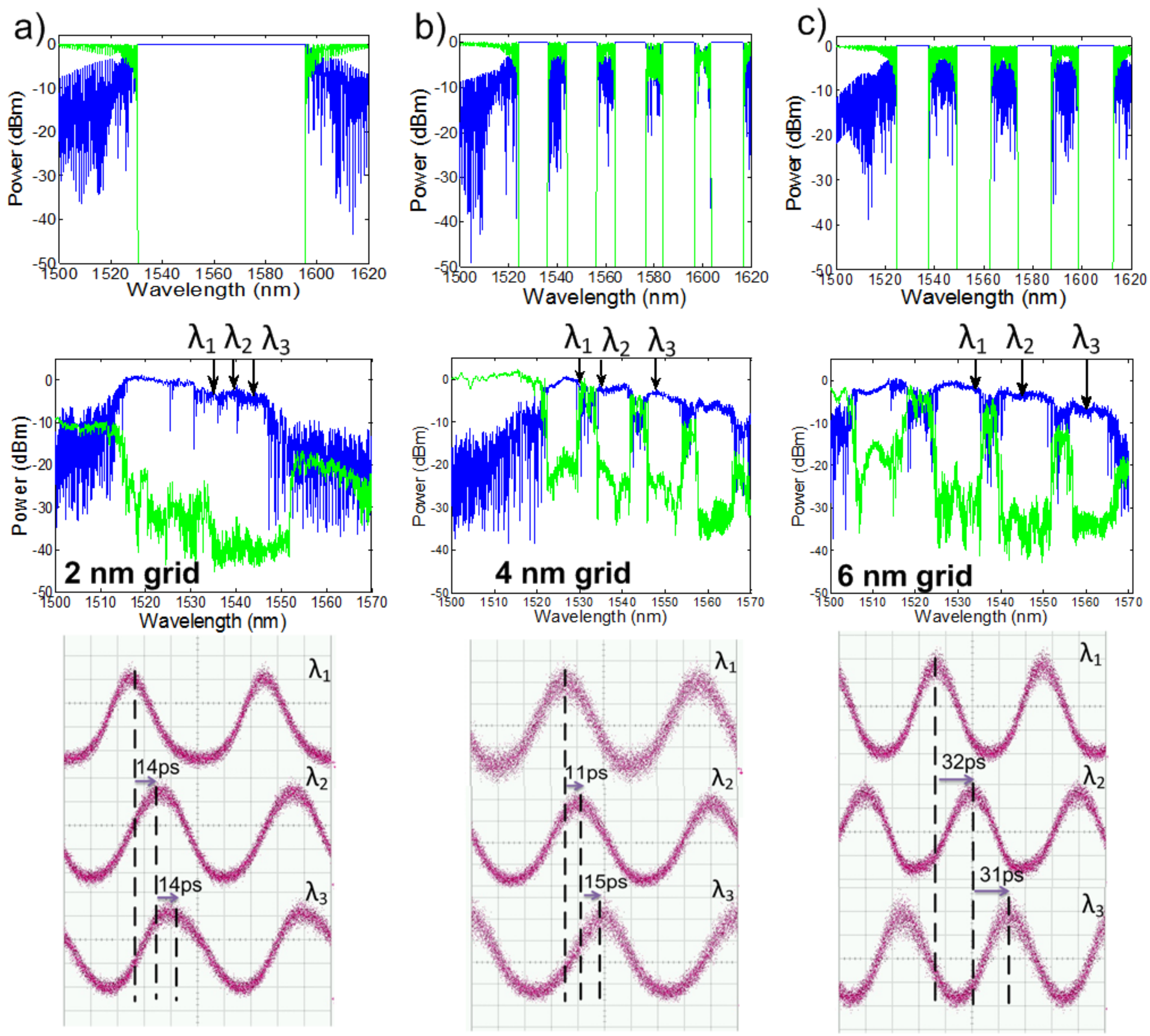

Fig. 4.11 Step-chirped sidewall Bragg gratings fabricated with 2, 4 and 6 nm grids with simulated (top) and experimental (bottom) spectra responses and corresponding sinusoidal signals delayed in time (20 ps/div): (a) $W_1 = 520$ nm, $\Delta W = 20$ nm, $\Lambda_1 = 310$ nm, $M = 6$ (20 ps/div) (b) $W_1 = 580$ nm, $\Delta W = 20$ nm, $\Lambda_1 = 302$ nm, $M = 5$ (20 ps/div) (c) $W_1 = 540$ nm, $\Delta W = 20$ nm, $\Lambda_1 = 304$ nm, $M = 4$ (25 ps/div). Simulations obtained with TMM implemented in MATLAB. Experimental spectra (transmission and reflection) recorded by Valentina Donzella at UBC.

2.5 nm. In Figure 4.12 (a) the width W_1 was reduced from 580 nm to 577 nm, while in Figure 4.12 (b) the width W_1 was reduced from 540 nm to 512 nm. Similar fit can be done with the other structures.

This proves that variations in width and corrugation depth can explain the differences in between expected and fabricated parameters and can be useful in future designs to compensate for lithographic limitations. The width variations as well as the waveguide thickness also affect the group refractive index causing the discrepancies in the group delays. However, the higher the grid resolution (i.e. 2 nm) the closer to the simulated results a design is approaching, suggesting that with the finer increments in the grating periods one can obtain desired delay with a sidewall structure. Some distortion of the signal is noticeable and is attributed to high ripples in the reflections bands. This can be reduced in the future by introducing apodization techniques.

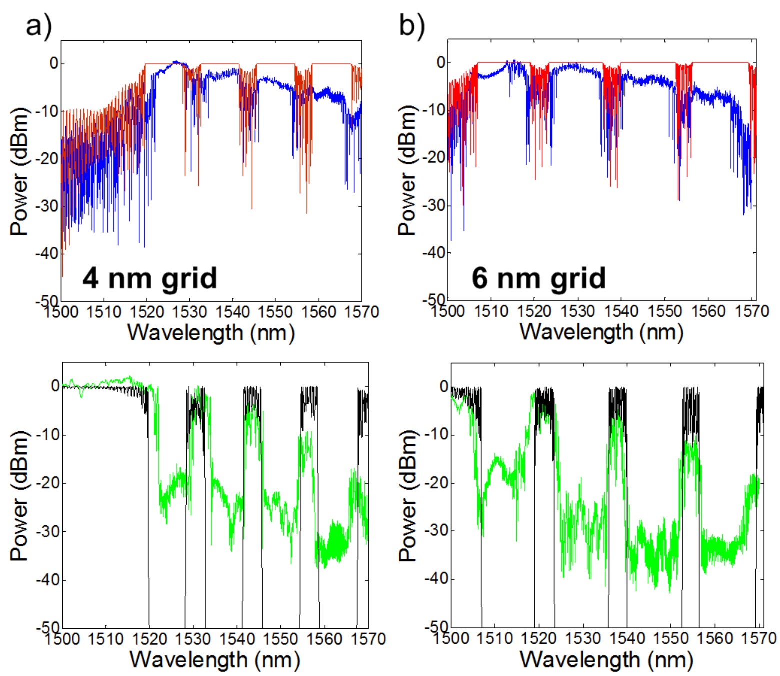

Fig. 4.12 Simulation fit to the experimental results for two step-chirped sidewall Bragg grating structures with adjusted width and corrugation depth: (a) $W_1 = 577$ nm, $\Delta W = 16$ nm (b) $W_1 = 512$ nm, $\Delta W = 16$ nm. Reflection: experimental (blue) vs. simulation (red). Transmission: experimental (green) vs. simulation (black).

4.5 Sidewall Bragg Gratings in SOI Summary

Chapter 4 demonstrates how optical delay lines can be implemented with sidewall gratings in silicon waveguides spanning relatively large delays of up to 90 ps and over wide bandwidths (33 to 72 nm). Two approaches were demonstrated and implemented, serial sidewall Bragg grating arrays and the step-chirped sidewall Bragg gratings, with both approaches showing better performance that is comparable to the simulated results when printed with a finer grid. Additionally many assumptions were made in the simulation process introducing uncertainties in the expected final results and more time should be invested in adjusting simulation approach to fit the fabrication process. Nevertheless, fabricated devices confirm that achieving large group delays through sidewall gratings is possible. However, sidewall grating structures also have to be tested for more complex signal processing including delaying modulated data where apodization techniques will have to be considered in order to reduce large ripples in the reflection bands that would distort the signal. Further optimization is needed if they are to be used in applications.

Chapter 5

Conclusion and Future Work

5.1 Summary

Integrated voice, video and data services that are becoming more widely employed by increasing number of users require very large bandwidths as well as increasing number of devices enabling the communication protocols. Besides satisfying the demand for bandwidth, the challenge also lies in building environment friendly networks with reduced print size and power consumption. Well established electronics platform has been fulfilling the bandwidth and speed requirements, however on account of increasing system complexity where scalability to higher data rates and lower power consumption started playing a leading role. Photonics based platforms gained in popularity with advances in technologies that bypass electronics' potentials with its high speed capabilities, multiple channel operation and reconfigurability. Different optical modulation schemes are being exploited with the best results achieved when combining them and using all of their advantages. Coherent detection systems that have been drawing increasing attention rely on OTDM and WDM modulations to enable very high serial data rates per single wavelength channel. Additionally, all-optical systems are being investigated for their obvious transparency to the increasing bit rate and ultra high speed capabilities that are not limited by electronic switches and routers, as well as for reduced number of amplifiers used across the network.

This thesis addressed photonics based platform and all-optical signal processing that can be implemented in nanoscale devices fabricated on silicon. It explored the advantages of all-optical OTDM demultiplexing scheme implemented in silicon waveguides. It investigated demultiplexing through using FWM phenomenon that can easily occur in suitably engineered waveguides. The thesis also proposed a design of optical delay lines implemented in silicon waveguides. It demonstrated how optical signals can acquire delays by propagating through relatively simple sidewall grating structures and ultimately suggesting how those structures can be used for all-optical demultiplexing purposes. It also indicated how OTDM demultiplexer can eventually be fully integrated on silicon-on-insulator.

In chapter 2 a brief overview of various techniques used for OTDM demultiplexing was given while motivating the FWM process employed in a highly nonlinear medium for its almost instantaneous nature suitable for ultra-fast switching and for its phase preserving capabilities suitable for many modulation formats. The chapter gave an overview of all the necessary building blocks for implementing a demultiplexer including generation of tunable optical delay line through FWM process and dispersion-conversion principle in the same nonlinear medium.

Chapter 3 introduced silicon waveguides as medium of choice noting the important parameters. Previously achieved results with OTDM demultiplexing implemented in HNLF were analyzed. Tunable optical delay line generation and demultiplexing process were successfully implemented bidirectionally in the same piece of HNLF thus reducing the component count. Both processes were based on FWM phenomenon. The same principles were used for OTDM demultiplexing experiment conducted in silicon waveguide though bidirectional propagation was not possible due to high coupling losses. Tunable optical delay line generation and demultiplexing process were implemented in two separate stages. Error free demultiplexing was achieved of 40 Gb/s-to-10 Gb/s OTDM signal while indicating the potential for scalability to higher data bit rates and different modulation formats as well as for combining the two stages bidirectionally when the losses are reduced.

In chapter 4 step-chirped waveguide Bragg gratings were introduced and characterized. The devices were designed and fabricated with incentive to replace the FBG used in the first stage of demultiplexing experiment. Sidewall grating structures were implemented with serial grating arrays and step-chirped gratings. Different configurations were attempted by varying waveguides widths, corrugation depth, grating period and fabrication grid resolution. Fabricated devices provided discrete delays in 11 ps to 32 ps steps across around 33 nm to 72 nm bandwidths. The design represented only the preliminary step toward implementing integrated tunable delay line. No appodization nor other optimization techniques were introduced.

5.2 Future Work Toward Designing Fully Integrated OTDM Demultiplexer

The work demonstrated in this thesis is primarily focused on OTDM demultiplexing technique through use of FWM phenomenon in highly nonlinear silicon waveguides with the main incentive to eventually build a fully integrated demultiplexer in silicon. With this work, the platform for future integration is presented indicating the further steps toward realization.

Optical tunable delay line generation and demultiplexing process were implemented in two separate stages due to high coupling losses into silicon waveguides. For joining the two steps through bidirectional propagation the losses will have to be reduced. This can be initially improved by using higher precision coupling stages: adding rotation stages permitting precise angle adjustment, adding translation stages with nanometer or smaller resolution, using tapered fiber tips. However, the smallest coupling loss to be achieved is only 30% efficient, thus, to further optimize coupling, more efficient grating couplers need to be considered. Recently, ultra low loss inverted taper couplers were designed and demonstrated in SOI with less than 1 dB loss per coupler [63]. The couplers were tapered from the waveguide width to less than 15 nm and then embedded in a polymer waveguide with a cross-sectional dimension matched to the access fibers, thus eliminating any misalignments. With reduced loss and with bidirectional propagation through silicon waveguides demultiplexing can be demonstrated for higher data bit rates, i.e. 80 Gb/s, 160 Gb/s. Furthermore, by exploiting FWM transparency to phase modulations different modulation formats can be implemented, i.e. DPSK, DQPSK. Additionally, optical tunable delay line generation relied on bulky FBG. For this device to be successfully replaced by a nanoscale waveguide Bragg grating, the presented design has to be improved. More detailed analysis of expected versus fabricated values can be conducted so that design can compensate for fabrication limitations. This includes using a more sinusoidal corrugation grating mask profile in the design to reduce the rounding effect and uncertainties in the corrugation depth values. Essentially, this translates to using more complex equations to evaluate corrugation depth and average effective refractive index when simulating Transfer Matrix Method. Moreover, the design should be intended for 2 nm or lower fabrication grid. With projected variations, device parameters can then be optimized to achieve desired delays, i.e. 25 ps delays for 40 Gb/s-to-10 Gb/s demultiplexing. Sidewall grating structures also have to be tested for more complex signal processing including delaying modulated data where apodization techniques will have to considered. Apodization can reduce large ripples in the reflection bands that distort the signal. Different techniques can be implemented directly on the sidewalls structures, however using coupled waveguides or gratings should offer a more robust solution. Sidewall grating structures represent a simple implementation of optical delay lines, but with current fabrication technology only discrete time delays can be achieved (the fabrication grid needed for some of initially desired results was beyond 1 nm). For more continuous functions, more complex designs should be considered (i.e. Figure 4.4 (b)). Finally, silicon waveguides and waveguide gratings will have to be fabricated on the same chip (simple schematic illustration is presented in Figure 5.1). This step will eliminate the need for many additional components, i.e. EDFAs, filters, and make the OTDM demultiplexing integrated and compact.

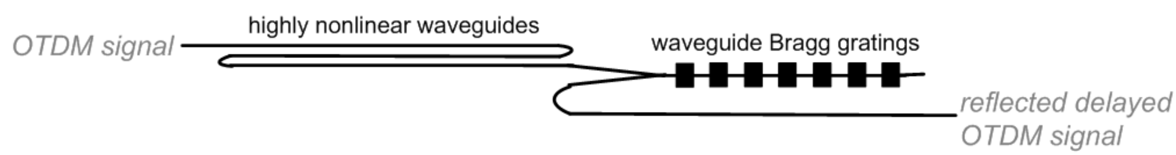

Fig. 5.1 Schematic diagram of an integrated OTDM demultiplexer.

References

[1] Cisco, “Living the Connected Life,” 2006. Information available at
http ://www.cisco.com/en/US/netsol/ns705/networking_solutions_solution.html.

[2] “Internet Usage Statistics: The Internet Big Picture.” Information available at
http ://www.internetworldstats.com/stats.htm.

[3] Cisco, “Cisco VNI Service Adoption Forecast, 2011-2016,” 2012. Information available at
http://www.cisco.com/en/US/solutions/collateral/ns341/ns525/ns537/ns705/ns1−186/Cisco_VNI_SA_Forecast_WP.html.

[4] Intel, “New Intel Server Technology: Powering the Cloud to Handle 15 Billion Connected Devices,” 2012. Information available at
http ://newsroom.intel.com/community/intel_newsroom/blog/2012/03/06/new − intel − server − technology − powering − the − cloud − to − handle − 15 − billion − connected − devices.

[5] “Strategies to Address Federal Data Center Consolidation and Cloud Computing,” 2012. Information available at
http ://blog.equinix.com/2012/06/strategies−to−address−federal−data−center−consolidation − and − cloud − computing/.

[6] Ericsson, “Optical innovation will meet operators’ future broadband demands,” 2012. Information available at
http ://www.ericsson.com/news/120330_optical_innovation_will_meet_operators_fu−ture_broadband_demands_244159020_c.

[7] Cisco, “Cisco Global Cloud Index: Forecast and Methodology, 2011-2016,” 2012. Information available at
http ://www.cisco.com/en/US/solutions/collateral/ns341/ns525/ns537/ns705/ns1−175/Cloud_Index_White_Paper.html.

[8] Intel, "Intel Technology Update: Building Secure Energy Efficient Clouds Today," 2012. Information available at $http://www-03.ibm.com/systems/data/flash/hu/storageforum2012/15.pdf$.

[9] H. Ishikawa, *Ultrafast all-optical signal processing devices*, vol. 258. Wiley Online Library, 2008.

[10] "Telstra Selects Ericsson for Optical Network Evolution," 2013. Information available at $http://www.fiberopticsonline.com/doc/telstra-selects-ericsson-for-optical-network-evolution-0001$.

[11] B. Hitz, "Intel turns to photonics to extend Moore's law," *Physics World*, pp. 12–13, 2009.

[12] G. Agrawal, "Fiber-Optic Communication Systems 3rd ed," 2002.

[13] G. Kramer and G. Pesavento, "Ethernet passive optical network (EPON): Building a next-generation optical access network," *Communications magazine, IEEE*, vol. 40, no. 2, pp. 66–73, 2002.

[14] S. J. Savory, "Digital coherent optical receivers: algorithms and subsystems," *Selected Topics in Quantum Electronics, IEEE Journal of*, vol. 16, no. 5, pp. 1164–1179, 2010.

[15] T. Richter, E. Palushani, C. Schmidt-Langhorst, R. Ludwig, L. Molle, M. Nolle, and C. Schubert, "Transmission of single-channel 16-QAM data signals at terabaud symbol rates," *Lightwave Technology, Journal of*, vol. 30, no. 4, pp. 504–511, 2012.

[16] M. Pasandi, "Adaptive decision-directed channel equalization and laser phase noise induced inter-carrier-interference mitigation for coherent optical orthogonal frequency division multiplexing transport systems." PhD thesis, 2012.

[17] A. P. Bianzino, C. Chaudet, D. Rossi, and J.-L. Rougier, "A survey of green networking research," *Communications Surveys & Tutorials, IEEE*, vol. 14, no. 1, pp. 3–20, 2012.

[18] Y. Zhang, P. Chowdhury, M. Tornatore, and B. Mukherjee, "Energy efficiency in telecom optical networks," *Communications Surveys & Tutorials, IEEE*, vol. 12, no. 4, pp. 441–458, 2010.

[19] R. S. Tucker, "Green optical communications-Part II: Energy limitations in networks," *Selected Topics in Quantum Electronics, IEEE Journal of*, vol. 17, no. 2, pp. 261–274, 2011.

[20] O. Wada, "Femtosecond all-optical devices for ultrafast communication and signal processing," *New Journal of Physics*, vol. 6, no. 1, p. 183, 2004.

[21] M. Saruwatari, "All-optical signal processing for terabit/second optical transmission," *Selected Topics in Quantum Electronics, IEEE Journal of*, vol. 6, no. 6, pp. 1363–1374, 2000.

[22] S. B. Yoo, "Photonic integration and optical interconnects for future communications, computing, and signal processing systems," in *SPIE OPTO: Integrated Optoelectronic Devices*, pp. 72210B–72210B, International Society for Optics and Photonics, 2009.

[23] B. Jalali and S. Fathpour, "Silicon photonics," *Lightwave Technology, Journal of*, vol. 24, no. 12, pp. 4600–4615, 2006.

[24] G. Lifante, *Integrated Photonics: Fundamentals*. Wiley Online Library, 2003.

[25] H.-G. Weber, R. Ludwig, S. Ferber, C. Schmidt-Langhorst, M. Kroh, V. Marembert, C. Boerner, and C. Schubert, "Ultrahigh-speed OTDM-transmission technology," *Journal of lightwave technology*, vol. 24, no. 12, pp. 4616–4627, 2006.

[26] G. P. Agrawal, *Nonlinear fiber optics*. Springer, 2000.

[27] A. E. Willner, B. Zhang, L. Zhang, L. Yan, and I. Fazal, "Optical signal processing using tunable delay elements based on slow light," *Selected Topics in Quantum Electronics, IEEE Journal of*, vol. 14, no. 3, pp. 691–705, 2008.

[28] P. Seddighian and L. R. Chen, "Independent and simultaneous delay control of two 10-Gb/s channels using a single optical delay element," *Photonics Technology Letters, IEEE*, vol. 21, no. 6, pp. 401–403, 2008.

[29] S. L. Jansen, M. Heid, S. Splter, E. Meissner, C. J. Weiske, A. Schpflin, D. Khoe, and H. De Waardt, "Demultiplexing 160 Gbit/s OTDM signal to 40 Gbit/s by FWM in SOA," *Electronics Letters*, vol. 38, no. 17, pp. 978–980, 2002.

[30] T. Ohara, H. Takara, I. Shake, K. Mori, K. Sato, S. Kawanishi, S. Mino, T. Yamada, M. Ishii, I. Ogawa, *et al.*, "160-Gb/s OTDM transmission using integrated all-optical MUX/DEMUX with all-channel modulation and demultiplexing," *Photonics Technology Letters, IEEE*, vol. 16, no. 2, pp. 650–652, 2004.

[31] E. Tangdiongga, Y. Liu, H. De Waardt, G. Khoe, A. Koonen, H. Dorren, X. Shu, and I. Bennion, "All-optical demultiplexing of 640 to 40 Gbits/s using filtered chirp of a semiconductor optical amplifier," *Optics Letters*, vol. 32, no. 7, pp. 835–837, 2007.

[32] J. Turkiewicz, E. Tangdiongga, G. Khoe, and H. de Waardt, "Clock recovery and demultiplexing performance of 160-Gb/s OTDM field experiments," *Photonics Technology Letters, IEEE*, vol. 16, no. 6, pp. 1555–1557, 2004.

[33] S. Kodama, T. Yoshimatsu, and H. Ito, "320 Gbit/s error-free demultiplexing using ultrafast optical gate monolithically integrating a photodiode and electroabsorption modulator," *Electronics Letters*, vol. 39, no. 17, pp. 1269–1270, 2003.

[34] H.-G. Weber, R. Ludwig, S. Ferber, C. Schmidt-Langhorst, M. Kroh, V. Marembert, C. Boerner, and C. Schubert, "Ultrahigh-speed OTDM-transmission technology," *Journal of lightwave technology*, vol. 24, no. 12, pp. 4616–4627, 2006.

[35] G. P. Agrawal, "Highly Nonlinear Fibers and Their Applications," 2007. Information available at
http://www.optics.rochester.edu/users/gpa/HNLF_1h.pdf.

[36] H. Sotobayashi, W. Chujo, and T. Ozeki, "80 Gbit/s simultaneous photonic demultiplexing based on OTDM-to-WDM conversion by four-wave mixing with supercontinuum light source," *Electronics Letters*, vol. 37, no. 10, pp. 640–642, 2001.

[37] Z.-Q. Hui and J.-G. Zhang, "Wavelength conversion, time demultiplexing and multicasting based on cross-phase modulation and four-wave mixing in dispersion-flattened highly nonlinear photonic crystal fiber," *Journal of Optics*, vol. 14, no. 5, p. 055402, 2012.

[38] M. Scaffardi, F. Fresi, G. Meloni, A. Bogoni, L. Poti, N. Calabretta, and M. Guglielmucci, "Ultra-fast 160: 10Gbit/s time demultiplexing by four wave mixing in 1m-long B_2O_3-based fiber," *Optics communications*, vol. 268, no. 1, pp. 38–41, 2006.

[39] K. G. Petrillo and M. A. Foster, "Full 160-Gb/s OTDM to 16x10-Gb/s WDM conversion with a single nonlinear interaction," *Optics express*, vol. 21, no. 1, pp. 508–518, 2013.

[40] E. Bodtker and J. Bowers, "Techniques for optical demultiplexing in high bit rate communication systems," *Lightwave Technology, Journal of*, vol. 13, no. 9, pp. 1809–1814, 1995.

[41] H. H. Mulvad, M. Galili, L. K. Oxenløwe, H. Hu, A. T. Clausen, J. B. Jensen, C. Peucheret, and P. Jeppesen, "Demonstration of 5.1 Tbit/s data capacity on a single-wavelength channel," *Opt. Express*, vol. 18, no. 2, pp. 1438–1443, 2010.

[42] H. Sotobayashi, C. Sawaguchi, Y. Koyamada, and W. Chujo, "Ultrafast walk-off-free nonlinear optical loop mirror by a simplified configuration for 320-Gbit/s time-division multiplexing signal demultiplexing," *Optics letters*, vol. 27, no. 17, pp. 1555–1557, 2002.

[43] H. Hansen Mulvad, L. Oxenlwe, M. Galili, A. Clausen, L. Gruner-Nielsen, and P. Jeppesen, "1.28 Tbit/s single-polarisation serial OOK optical data generation and demultiplexing," *Electronics Letters*, vol. 45, no. 5, pp. 280–281, 2009.

[44] M. Pelusi, V. Ta'Eed, M. Lamont, S. Madden, D.-Y. Choi, B. Luther-Davies, and B. Eggleton, "Ultra-High Nonlinear As_2S_3 Planar Waveguide for 160-Gb/s Optical Time-Division Demultiplexing by Four-Wave Mixing," *Photonics Technology Letters, IEEE*, vol. 19, no. 19, pp. 1496–1498, 2007.

[45] F. Li, M. Pelusi, B. J. Eggleton, A. Densmore, R. Ma, S. Janz, D. Xu, and D. J. Moss, "Error-free all-optical demultiplexing at 160Gb/s via FWM in a silicon nanowire," in *Conference on Lasers and Electro-Optics*, Optical Society of America, 2010.

[46] H. Ji, M. Pu, H. Hu, M. Galili, L. K. Oxenlowe, K. Yvind, J. M. Hvam, and P. Jeppesen, "Optical waveform sampling and error-free demultiplexing of 1.28 Tb/s serial data in a nanoengineered silicon waveguide," *Lightwave Technology, Journal of*, vol. 29, no. 4, pp. 426–431, 2011.

[47] P. Seddighian, K. Ramaswamy, and L. R. Chen, "Optical tunable delay for OTDM demultiplexing with reduced component count," in *Optical Communications and Networks (ICOCN 2010), 9th International Conference on*, pp. 212–214, IET, 2010.

[48] R. Kashyap, *Fiber bragg gratings*. Academic Press, 2010.

[49] B. E. Saleh and M. C. Teich, *Fundamentals of photonics*, vol. 32. Wiley-Interscience Hoboken, NJ, 2007.

[50] A. Yariv, "Coupled-mode theory for guided-wave optics," *Quantum Electronics, IEEE Journal of*, vol. 9, no. 9, pp. 919–933, 1973.

[51] R. Kashyap, P. F. McKee, R. J. Campbell, and D. L. Williams, "Novel method of producing all fibre photoinduced chirped gratings," *Electronics Letters*, vol. 30, no. 12, pp. 996–997, 1994.

[52] T. Erdogan, "Fiber grating spectra," *Lightwave Technology, Journal of*, vol. 15, no. 8, pp. 1277–1294, 1997.

[53] K. Hill, Y. Fujii, D. Johnson, and B. Kawasaki, "Photosensitivity in optical fiber waveguides: Application to reflection filter fabrication," *Applied Physics Letters*, vol. 32, p. 647, 1978.

[54] K. Okamoto, *Fundamentals of optical waveguides*. Academic press, 2010.

[55] M. J. Strain and M. Sorel, "Design and fabrication of integrated chirped Bragg gratings for on-chip dispersion control," *Quantum Electronics, IEEE Journal of*, vol. 46, no. 5, pp. 774–782, 2010.

[56] I. Giuntoni, D. Stolarek, D. I. Kroushkov, J. Bruns, L. Zimmermann, B. Tillack, and K. Petermann, "Continuously tunable delay line based on SOI tapered Bragg gratings," *Optics Express*, vol. 20, no. 10, pp. 11241–11246, 2012.

[57] C. Lin, J. R. Adleman, E. Jacobs, J. Rodgers, R. Liang, T. Chen, and A. Fitting, "Higher order planar-waveguide Bragg grating on curved waveguide," in *Photonics Conference (PHO), 2011 IEEE*, pp. 357–358, IEEE, 2011.

[58] D. Tan, K. Ikeda, and Y. Fainman, "Coupled chirped vertical gratings for on-chip group velocity dispersion engineering," *Applied Physics Letters*, vol. 95, no. 14, pp. 141109–141109, 2009.

[59] F. Morichetti, A. Melloni, C. Ferrari, and M. Martinelli, "Error-free continuously-tunable delay at 10 Gbit/s in a reconfigurable on-chip delay-line," *Optics Express*, vol. 16, no. 12, pp. 8395–8405, 2008.

[60] L. Chrostowski and M. Hochberg, *Silicon Photonics Design*, vol. draft, pp. 26–27. 2012.

[61] X. Wang, W. Shi, R. Vafaei, N. A. Jaeger, and L. Chrostowski, "Uniform and sampled bragg gratings in soi strip waveguides with sidewall corrugations," *Photonics Technology Letters, IEEE*, vol. 23, no. 5, pp. 290–292, 2011.

[62] X. Wang, W. Shi, R. Vafaei, N. A. Jaeger, and L. Chrostowski, "Silicon-on-insulator bragg gratings fabricated by deep uv lithography," in *Communications and Photonics Conference and Exhibition (ACP), 2010 Asia*, pp. 501–502, IEEE, 2010.

[63] M. Pu, L. Liu, H. Ou, K. Yvind, and J. M. Hvam, "Ultra-low-loss inverted taper coupler for silicon-on-insulator ridge waveguide," *Optics Communications*, vol. 283, no. 19, pp. 3678–3682, 2010.